AGU PUBLICATIONS

JGR

Journal of Geophysical Research: Oceans

RESEARCH ARTICLE

10.1002/2013JC009213

Key Points:
- Field application of a nearshore EnKF data assimilation system
- Remote sensing data are assimilated to improve model bathymetry
- After assimilating data, model prediction of a rip current is also improved

Correspondence to:
G. W. Wilson,
greg.wilson@dal.ca

Citation:
Wilson, G. W., H. T. Özkan-Haller, R. A. Holman, M. C. Haller, D. A. Honegger, and C. C. Chickadel (2014), Surf zone bathymetry and circulation predictions via data assimilation of remote sensing observations, *J. Geophys. Res. Oceans*, *119*, 1993–2016, doi:10.1002/2013JC009213.

Received 14 JUNE 2013
Accepted 25 FEB 2014
Accepted article online 3 MAR 2014
Published online 17 MAR 2014

Surf zone bathymetry and circulation predictions via data assimilation of remote sensing observations

G. W. Wilson[1], H. T. Özkan-Haller[1], R. A. Holman[1], M. C. Haller[2], D. A. Honegger[2], and C. C. Chickadel[3]

[1]College of Earth, Ocean, and Atmospheric Sciences, Oregon State University, Corvallis, Oregon, USA, [2]School of Civil and Construction Engineering, Oregon State University, Corvallis, Oregon, USA, [3]Applied Physics Laboratory, University of Washington, Seattle, Washington, USA

Abstract Bathymetry is a major factor in determining nearshore and surf zone wave transformation and currents, yet is often poorly known. This can lead to inaccuracy in numerical model predictions. Here bathymetry is estimated as an uncertain parameter in a data assimilation system, using the ensemble Kalman filter (EnKF). The system is tested by assimilating several remote sensing data products, which were collected in September 2010 as part of a field experiment at the U.S. Army Corps of Engineers Field Research Facility (FRF) in Duck, NC. The results show that by assimilating remote sensing data alone, nearshore bathymetry can be estimated with good accuracy, and nearshore forecasts (e.g., the prediction of a rip current) can be improved. This suggests an application where a nearshore forecasting model could be implemented using only remote sensing data, without the explicit need for in situ data collection.

1. Introduction

The surf zone is defined as the coastal region where the effects of wave breaking dominate the hydrodynamics. It is often characterized by large waves and strong currents, as well as a sandy, mobile bottom, and hence can be a challenging or even hazardous environment for in situ observation. Because of this, remote sensing is a valuable tool for long-term monitoring of the nearshore; for a recent review, see *Holman and Haller* [2013]. A common approach has been optical imagery collected from shore-based towers, such as the Argus Network [*Holman and Stanley*, 2007]. Others method include radar [*Puleo et al*., 2003; *Catalán et al*., 2011; *Haller et al*., 2013], infrared [*Chickadel et al*., 2009, and as discussed herein], LIDAR [*Blenkinsopp et al*., 2012], and airborne platforms [*Dugan et al*., 2001]. Furthermore, image processing techniques are increasingly being used to extract quantitative hydrodynamic observations from surf zone imagery, using particle image velocimetry [*Holland et al*., 2001; *Puleo et al*., 2003], stereo-video [*de Vries et al*., 2011; *Palmsten and Holman*, 2011], and other techniques discussed herein.

A common factor among all the above measurement techniques is the ability to sample a broad spatial and temporal range, compared to traditional in situ instruments (e.g., bottom-mounted gages and profilers). The trade-off, however, is usually in terms of measurement uncertainty ("noise") and/or the inability to sample continuous high-quality data at a fixed location ("sparseness"). Hence, the use of such data requires an ability to filter sparse and noisy observations. Data assimilation is a powerful approach to this problem where one seeks to utilize the information contained in observations (including their uncertainty), combined with a model for physical processes, to generate a statistical estimate of an unknown variable.

The use of data assimilation requires knowledge or assumptions regarding the uncertainty of observations, and, importantly, the uncertainty of the model. For instance, the first application of data assimilation in the surf zone by *Feddersen et al*. [2004] assumed errors were present in the model forcing, boundary conditions, and drag coefficient. Herein, it is assumed that model errors are caused solely by errors in bathymetry. Further, the bathymetry is assumed quasi-steady, i.e., constant over a 1/2 h observation window, and incremental corrections are derived within such windows. Treating bathymetry as the only source of error in the model is a simplifying approximation, but it is motivated by the fact bathymetry error often dominates the overall model error in practice. In particular, observations have shown significant bathymetric change can occur on time scales of days [*Lippmann and Holman*, 1990], and this has been demonstrated to cause large model errors if not measured or otherwise accounted for [*Wilson et al*., 2010]. Indeed, bathymetry error has

been specifically cited as a fundamental barrier to overall model accuracy in operational studies [*Allard et al*., 2008; *Austin et al*., 2012].

Using data assimilation for estimating bathymetry has been the focus of a number of recent studies in nearshore and other shallow water environments. *van Dongeren et al*. [2008] and *Holman et al*. [2013] have applied Kalman filtering schemes to assimilate pseudoobservations of depth (i.e., observations derived from an explicit depth-inversion) from remote sensing, with excellent results. Others have implemented more complex data assimilation schemes, including variational [*Zaron et al*., 2011; *Kurapov and Özkan-Haller*, 2013], and ensemble-based [*Wilson et al*., 2010; *Wilson and Özkan-Haller*, 2012; *Landon et al*., 2013], which are capable of assimilating general observations such as currents, wave height, etc. The work of *Wilson et al*. [2010] can be viewed as a precursor to the present study. They showed that bathymetric errors could be corrected using single-time observations of wave heights and alongshore currents from an in situ instrument array. Here their methods are extended to assimilate time-dependent remote sensing observations, a more realistic scenario for operational use. The results show bathymetric errors can be successfully controlled using remote sensing data alone, and this leads to significant improvement in the ability of the model to predict surf zone currents.

2. Observations

2.1. Experiment Overview

Observations were collected during a field experiment in September 2010 at the U.S. Army Corps of Engineers (USACE) Field Research Facility (FRF) in Duck, NC, as part of the data assimilation and remote sensing for Littoral Applications field program funded by the Office of Naval Research [*Jessup et al*., 2012]. The study domain encompassed 1 km of a sandy barrier island beach, from the shore to 8 m water depth (~800 m offshore). Figure 1 shows the experimental layout, including the locations of in situ instruments and the footprints of remote sensing observations described in this section.

Table 1 summarizes the remote sensing observations (i.e., the data which will be assimilated, see sections 2.3–2.5) in terms of their spatial resolution, and the window size over which they are derived. Note the observation errors listed in Table 1 are averaged values based on the data presented in section 4.3; when assimilating data, each data point is assigned an observation error value which is computed as part of the data extraction process.

2.2. In Situ Data

Bathymetry at the FRF has been surveyed regularly (approximately fortnightly) since 1981 using the USACE's CRAB [*Birkemeier*, 1984] and Light Amphibious Resupply Craft (LARC). A standard bathymetric survey consists of across-shore transects at roughly 50 m spacing alongshore. Two LARC surveys were performed around the time of the present experiment, on 6 and 15 September. These data will be used for validation of the bathymetry estimation routine in section 4. Additionally, 253 archived surveys (1981 to July 2010) were used to calculate a climatological bathymetry which serves as an initial state for the data assimilation system (see section 4). When necessary (for visual presentation, and for forward modeling), we interpolated the September raw data to our model grid using bilinear interpolation followed by a spatial smoothing filter.

Measurements of the incoming waves at the offshore model boundary ($x = 900$ m, about 8 m depth) are also provided by the FRF, using an array of 15 bottom-mounted pressure sensors, referred to as the 8 m array [*Long*, 1996]. These data are processed to form estimates of frequency-directional wave spectra, reported every 3 h.

Three bottom-mounted colocated pressure and acoustic-Doppler current profilers were positioned on the transect $y = 940$ m [*Mulligan et al*., 2010], and a bottom-mounted acoustic-Doppler current profiler at $(x, y) = (191, 714)$ m. These are used for verification of remote sensing observations in section 4.1.

2.3. Optical Remote Sensing

Optical remote sensing data were collected from an Argus station, consisting of five video cameras mounted on a 43 m tower located at $(x, y) = (32, 590)$ m. The combined field of view covers the full alongshore extent of the study site, and extends out to $x = 500$ m. Pixel resolution degrades with distance from

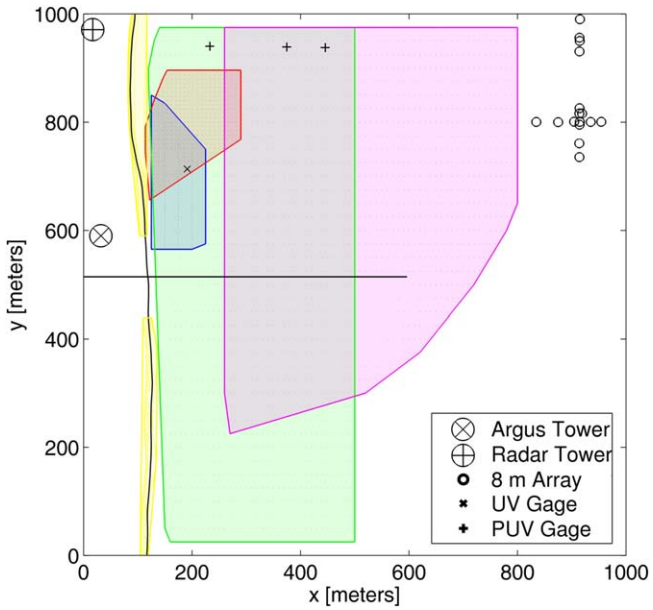

Figure 1. Map of 2010 field experiment, showing locations of in situ and remote sensing data in standard FRF coordinates. Location of shoreline and FRF pier are plotted as black lines for reference (offshore is in the positive—*x* direction). In situ data consist of 8 m array pressure gages (°), colocated FRF pressure and current-profiling instruments (PUV Gage) (+), and standalone current profiler (UV Gage) (×). Remote sensing data, from Argus tower (⊗) and radar tower (⊕), consist of Optical Current Meter (blue), Infrared PIV (red), EO-k (green), EM-k (magenta), and shoreline (yellow).

the tower, ranging from 0.25 to 10 m. The cameras recorded data in 17 min bursts, sampling at 2 Hz, starting every 1/2 h during daylight hours.

2.3.1. Shoreline Identification (EO-xs)

The location of the shoreline was estimated as a function of *y* using the most-shoreward local maximum of image variance. This data will be referred to as EO-xs (for "electro-optical shoreline"). The methodology for extracting the shoreline follows *Plant and Holman* [1997], except in the present case variance imagery was found to give better shoreline estimates than time-mean imagery. Initially, shoreline estimates were extracted automatically with fair success; however, manual corrections were sometimes required in cases with uneven lighting or irregular wave breaking patterns. The data were also smoothed using a quadratic Loess interpolation having an alongshore window span of 100 m. A conservative user-defined error estimate of 10 m standard deviation in *x* was assigned across all data.

2.3.2. Optical Current Meter (EO-v)

The Optical Current Meter technique, developed by *Chickadel et al*. [2003] (hereafter, CHF), was used for measuring alongshore currents from optical imagery. This data will be referred to as EO-v. Five alongshore transects of pixels were used, spaced 25 m in the across-shore, starting at $x = 125$ m. Time-stacks from these

Table 1. Summary of Remote Sensing Data Sources[a]

Observation	Variable	Δx (m)	Δy (m)	Δt (h)	l_x (m)	l_y (m)	*rms* (σ_d)
EO-xs	x_{shore}	n/a	1	1	n/a	30	10 m
EO-v	v	25	5	0.5	n/a	15	39 cm/s
IR-v	v	8	8	0.5	8	8	47 cm/s
EO-k	k	10	25	0.5	20	50	0.072 rad/m
EM-k	k	10	25	1	20	50	0.039 rad/m

[a]"Observation" is the name used in the text to describe the observation, "Variable" is the model variable that is observed/assimilated, (Δx, Δy) are the spatial resolution, Δt is the time between observations, (l_x, l_y) are the half-widths of the rectangular analysis window over which the observation is computed, and *rms* (σ_d) are the root-mean-square values of predicted observation error, for all observations used in the experiment of section 4.3. In the case of shoreline observations, an effective sampling window is defined based on the spatial smoothing applied to the observations.

transects were analyzed using the method of CHF, which uses a parametric spectral fit to extract slow-moving features in the imagery. Such features are usually associated with drifting foam, which CHF showed is a good proxy for alongshore current. Quality control also follows CHF, and additionally estimates were excluded if the raw data alongshore pixel spacing was greater than 1 m. The CHF method includes an estimate of measurement error for each observation point.

2.3.3. Wave Celerity (EO-k)

Wave properties were estimated from optical data using a spectral algorithm developed by *Plant et al*. [2008] and recently extended by *Holman et al*. [2013]. This algorithm extracts measurements of the wave number (scalar) and wave angle at four frequency bands per location. Only the wave number data will be assimilated, and it will be referred to as EO-k. Assimilation of wave angle data is possible in principle, but was not successful in the present experiment: difficulties were encountered related to the directional spread of waves.

Quality control for EO-k follows *Holman et al*. [2013], except the threshold for phase-map fit skill was increased from 0.5 (default) to 0.75, and data were excluded if the analysis window included subaerial (dry) points (based on the identified shoreline, section 2.3.1). Measurement error is extracted separately for each data point.

2.4. Infrared Remote Sensing: Particle Image Velocimetry (IR-v)

An infrared video camera, similar to the system used by *Chickadel et al*. [2009], was also deployed on the FRF tower during this experiment. This imagery (pixel resolution of order 1 m) was analyzed in 30 min bursts using particle image velocimetry (PIV) to extract measurements of time-averaged velocity, referred to as IR-v. The incident wave signal was removed from the imagery prior to processing by extracting the minimum pixel intensity over a moving 10 s window. It is assumed the tracked features correspond to remnant foam (which is typically cooler than surface water and/or recently generated foam), and remnant/active coherent structures, both of which are generated by wave breaking and are passively advected by mean currents.

Quality control was defined by excluding measurements for which the PIV algorithm used fewer than 30 samples within its 30 min analysis window. Also, measurements were excluded if they were within 20 m of the shoreline, such that the PIV analysis window did not contain subaerial points. The PIV algorithm estimates measurement error for each observation point. Finally, although this method measures both x and y components of current, only the alongshore current will be assimilated. The numerical model used here is not designed to reproduce the stronger depth-variability expected in the across-shore current.

2.5. Radar Remote Sensing: Wave Celerity (EM-k)

An X-band marine radar, described by *Haller et al*. [2013], was mounted at the location $(x, y, z) = (17, 971, 14)$m. The system measured backscatter intensity in range bins spaced at 3 m to a maximum range of 927 m, and 270 azimuthal bins. Data were collected at the top of each hour, and each collection consisted of 760 antenna rotations at a rate of 46 rotations per minute (17 min total).

The imaging mechanism for X-band radar is scattering from centimeter-scale sea surface roughness, for example, due to wind or wave breaking. This signal is modulated by incident wave slope, resulting in a strong wave signal in the imagery. Wavefield information could therefore be extracted using the same routine as used for the optical data, section 2.3.3 (the same analysis windows and output resolution was used). This data will be referred to as EM-k (EM for "electromagnetic").

3. Modeling and Bathymetry Inversion System

The inverse modeling system comprises a deterministic forward model, and a data-assimilating inverse model used to estimate bathymetry. The methodology follows *Wilson et al*. [2010], but includes extensions for time-varying sequential assimilation and hence implements the ensemble Kalman filter (EnKF) *Evensen* [2006]. It also uses a slightly different forward model. The basic procedure is outlined below, and in Figure 2:

1. Define an initial background ensemble consisting of 200 realizations of bathymetry.

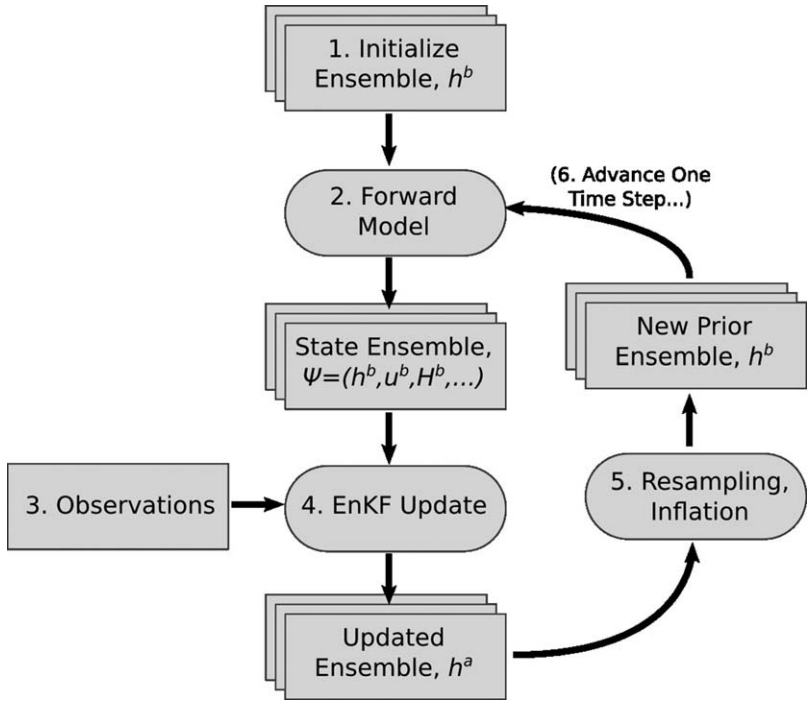

Figure 2. Flow diagram of time-dependent sequential assimilation scheme (numbers correspond to steps outlined in text).

2. For each member of the ensemble, apply the forward numerical model with fixed boundary conditions for the target observation time.

3. Define the observational data set for the target time (which includes measurement uncertainty), and extract corresponding predictions from the ensemble.

4. Apply the EnKF update equations with state augmentation, to assimilate the observations and thereby obtain an updated ensemble of bathymetry.

5. Adjust the ensemble spread to account for unresolved sediment transport and potential shortcomings of the filter, and resample to replace any failed ensemble members.

6. Move to the next observation time, and repeat from step 2.

Application of multiple assimilation cycles (defined as one iteration of steps 2–5) over time should refine the ensemble of bathymetry such that its distribution represents an improved state of knowledge given the observations. The mean of the ensemble will represent an estimate of the true bathymetry, and the covariance will represent the expected uncertainty of that estimate. This will be tested in section 4. In addition, a forward model run using this improved bathymetry is expected to give improved predictions of other variables such as currents; this is tested in section 4.4.

3.1. Forward Model

The numerical model SWAN [*Booij et al.*, 1999] is used to simulate incident waves, and the Regional Ocean Modeling System (ROMS) [*Shchepetkin and McWilliams*, 2005]; used here in depth-averaged 2-D mode) is used to simulate time-averaged currents. The model domain extends from the 10 cm depth contour (i.e., the shoreline, $x \approx 100$ m) to an offshore boundary $x = 900$ m, and for an alongshore span $-105 < y < 1410$ m (cf. Figure 1). Model grid spacing is 10 m (across-shore) by 15 m (alongshore), which was chosen to balance the need for accurate modeling of time-averaged flows (rip currents, alongshore current jet) with the need for large number of ensemble members. The domain is assumed periodic in the y direction, and the area $1110 < y < 1410$ m is used as a buffer zone over which the bathymetry is smoothly ramped to satisfy periodicity (the buffer zone is reapplied each time bathymetry is updated via data assimilation). The model

is reinitialized from rest for each observation period; continuous simulation would be problematic, because the model bathymetry changes abruptly each time data are assimilated.

The wave part of the model, SWAN, solves the stationary conservation of wave action equation [*Mei*, 1983], which governs transformation of wave energy (i.e., the frequency-directional wave spectrum) from the offshore boundary to the shoreline. Stationary offshore boundary conditions are specified for each model run using in situ measurements (see section 2), which are assumed alongshore uniform and are interpolated in time using the internal SWAN routine. Energy dissipation due to wave breaking is included using the parameterization of *Battjes and Janssen* [1978], with default physical constants in SWAN. The effect of currents on waves is not included, so that SWAN runs as a stand-alone model.

Wave spectral predictions from SWAN are then used to compute radiation stress gradients, which are passed as a static input to ROMS. The effect of wave rollers [*Svendsen*, 1984] is included following *Reniers et al*. [2004].

ROMS, in turn, solves the Reynolds-averaged hydrostatic Navier-Stokes equations, which are also averaged in depth and in time, over the time scale of waves (this time averaging produces the radiation stress gradient terms noted above). The model is allowed to spin-up for 7 h, and then model outputs are averaged over 30 min to simulate an observational data collection period. Boundary conditions are no-slip at the shoreline (10 cm depth) and radiation at the offshore boundary. Bottom stress is parameterized following *Svendsen and Putrevu* [1990], with a drag coefficient $f_w = 0.0053$ chosen based on a spatially averaged analysis of field data on this beach by *Feddersen and Guza* [2003]. Wind stress is included using the parameterization of *Smith* [1988], using wind velocity measurements from the offshore end of the FRF pier and assuming nominal values for air temperature, 10°C, and density, 1.22 kg/m^3. Horizontal momentum mixing is modeled using a harmonic mixing term, with a spatially dependent eddy viscosity parameterized for the surf zone following *Haas et al*. [2003]. Tidal elevation is treated quasi-statically (i.e., as a spatially constant offset in mean water level), and is defined using measurements from the end of the FRF pier. Note the inclusion of tidal measurements implies the goal of the assimilation is to estimate bathymetry relative to a constant vertical datum, rather than estimate total water depth versus time.

An example of long-term validation of a model with similar physical assumptions and parameterizations is given by *Ruessink et al*. [2001], who found ca. 10–20 cm/s accuracy in alongshore current (one of the variables assimilated in this study). Predictions of across-shore current are likely to be less accurate, because of the strong influence of depth-dependence which has been neglected; this has been investigated in recent modeling studies by *Haas and Warner* [2009], *Uchiyama et al*. [2010], and *Kumar et al*. [2011, 2012]. Additionally, model accuracy may be reduced in the presence of rip currents, due to an increased importance of depth-dependence [*Haas and Svendsen*, 2002], and wave-current interaction [*Haas et al*., 1998; *Yu and Slinn*, 2003]. Hence, inclusion of depth-dependence and wave-current interaction would be worthwhile extensions of the present work.

3.2. Mathematical Statement of Inverse Problem

Consider a state vector ψ, consisting of a concatenation of all the relevant variables in the model (i.e., h, u, v, k, etc.), including bathymetry, for all model grid points. The dimensions of ψ are $M \times 1$, where M is the total number of model variables (all of the model state variables at all grid points). Also define a vector of observations, d, having dimensions $K \times 1$ (K being the number of observations), and a $K \times M$ matrix L which serves to map ψ to the observation space. For example, if d comprises a list of observations of the velocity u at specific locations, then $L\psi$ represents interpolation of the model u to those locations.

The inverse problem can then be stated as: estimate the bathymetry h, given the observations d, and given the forward model for computing ψ given h. To regularize this under-determined problem, a "background" model state ψ^b and its covariance C_b is defined. The solution is then defined as the minimum of:

$$J[\psi] = \left(\psi - \psi^b\right)^T C_b^{-1} \left(\psi - \psi^b\right) + (d - L\psi)^T C_d^{-1} (d - L\psi), \tag{1}$$

(the superscript T denotes matrix transpose).

3.3. Definition of Background State

Following *Wilson et al*. [2010], the background covariance is constructed using an ensemble approximation [*Evensen*, 2006]. For the initial assimilation step, $N = 200$ realizations of bathymetric perturbations are computed using the Fourier Transform method described in *Evensen* [2006] (Fortran code available from enkf.nersc.no), which draws from the covariance:

$$C_h(\Delta x, \Delta y) = \sigma_h^2 \exp\left[-\left(\frac{\Delta x^2}{L_x^2} + \frac{\Delta y^2}{L_y^2}\right)\right], \tag{2}$$

where L_x, L_y, and σ_h are user-specified across-shore, alongshore, and vertical length scales, which dictate the amplitude and smoothness of bathymetric updates. These perturbations are then added to a user-specified initial background estimate of bathymetry h^b (e.g., see section 4.3) to form a bathymetry ensemble. By executing the forward model (section 3.1) for each member of this ensemble, one obtains an ensemble of full model state vectors, denoted ψ_i^b. Its sample mean is used for ψ^b, and the sample covariance is used for C_b. After the first assimilation step, the ensemble evolves via assimilation of data alone (section 3.4), and equation (2) is no longer used.

A common issue with ensemble-based covariance approximations is the potential for spurious long-range spatial correlations. Hence, following *Hamill et al*. [2001], all sample covariances are localized using a Schur product with a compactly supported correlation function. The correlation function used here is the same as used by *Hamill et al*. [2001], with a length scale of 75 m. This yields a cutoff separation distance of roughly 150 m beyond which all covariances are effectively set to zero. Note this also limits the ability of the system to develop long decorrelation lengths in C_{hh} as more data are assimilated over time, even if they exist in reality. This is a general limitation of the ensemble-based technique compared to exact adjoint-based schemes [e.g., *Feddersen et al*., 2004; *Zaron et al*., 2011; *Kurapov and Özkan-Haller*, 2013].

It bears mentioning that h has not been constrained to be strictly positive. This is physically acceptable, as negative water depth can simply be interpreted as dry land. Indeed, negative depths must be allowed very close to shore, so that the location of the shoreline can be corrected. However, negative depths are problematic if they occur in locations where waves or currents were measured. In that case, it is not possible to "measure" the ensemble as required in the assimilation process (section 3.5). To avoid this issue, a rule is defined that only one zero-crossing of still-water-depth may occur for any given y location, meaning the shoreline is a single-valued function of y, and no "islands" are allowed. This rule is enforced by truncating depths to a minimum value of 0.25 m, at all points offshore of the first zero-crossing. In cases, where truncation would cause a change in depth of more than 0.5 m, the realization is completely removed from the ensemble. If after these changes a given observation is still not measurable across all of the ensemble members (which occurred for some data near the shoreline), that observation is removed from the assimilation process. For the experiment of section 4.3, the above rules caused depths to be truncated in 4.1% of realizations, 0.5% of realizations had to be discarded, and 3.5% of the available data were discarded. Hence, in the present case the treatment of negative depths was not a major issue. However, future applications may benefit from more sophisticated treatment of negative depth, for example, by incorporating anamorphosis transforms such as the lognormal transform [*Bocquet et al*., 2010] or the ensemble-based transform of Béal *et al*. [2010].

3.4. Update Step

A formal minimization of the cost function equation (1) [e.g., *Evensen*, 2006; *Bennett*, 2002] gives the following equation for the updated state (or "analysis"):

$$\psi^a = \psi^b + C_b L^T \left(L C_b L^T + C_d\right)^{\dagger} \left(d - L\psi^b + e\right), \tag{3}$$

where the superscript † indicates a Moore-Penrose matrix inverse, which accounts for possible conditioning problems when the number of observations is larger than the ensemble size [*Evensen and van Leeuwen*, 1996]. Equation (3) is applied to each member of the prior ensemble, producing an updated ensemble of state vectors (with updated sample covariance). The analysis bathymetry, h^a, is extracted by selecting the appropriate rows of ψ^a (recall, ψ is a concatenation of all model state variables). Note random measurement

perturbations e_i are included for each member, with mean zero and covariance C_d, so that the analysis ensemble has the correct covariance [*Houtekamer and Mitchell*, 1998].

3.5. Observation Operator, *L*

Rather than explicitly specify the matrix L, each observed variable is extracted from the model (i.e., measured) using a set algorithm, described below. This reveals a minor abuse of notation in equation (3) in cases where the measurement process is nonlinear. In actual fact, $L\psi_i^b$ is implemented as $L(\psi_i^b)$, where L is a function (possibly nonlinear) which maps to the observation space. Similarly, C_bL^T is defined as the sample covariance (including localization) between ψ_i^b and $L(\psi_i^b)$ (and similarly for LC_bL^T). The function L is described next for each observation type (see section 2, for a description of the actual observations).

Measurements of currents are treated simply by linearly interpolating the predicted u and v from the model grid to the observation locations. This is the simplest of observation operators, because the forward model already outputs u and v explicitly.

Wave number measurements are defined using a submodel for wave dispersion, applied as a function of depth, waves and currents. Following the recommendation of *Catalán and Haller* [2007], the dispersion relationship of *Kirby and Dalrymple* [1986] (hereafter KD86) is used:

$$\left(\sigma-\vec{k}\cdot\vec{u}\right)^2=gk\left(1+f_1\epsilon^2E\right)\tanh\left(kD+f_2\epsilon\right), \tag{4}$$

where

$$\epsilon=\frac{kH}{2},\qquad E=\frac{8+\cosh 4kD-2\tanh^2 kD}{8\sinh^4 kD},$$

$$f_1(kD)=\tanh^5 kD,\qquad f_2(kD)=\left(\frac{kD}{\sinh kD}\right)^4.$$

In these equations, σ is the radial wave frequency, $\vec{k}$ is the wave number, H is the wave height, and D is the mean total water depth. The variables σ, H, D, and $\vec{u}$ are all spatially averaged over the remote sensing analysis window before computing $\vec{k}$. The KD86 model includes the effect of currents on waves, as well as the effect of finite wave amplitude. Note these effects are not included in SWAN, hence the use KD86 in the inversion step is somewhat ad hoc. Inclusion of currents' effects on waves in the forward model is possible, but was not done for computational efficiency reasons; inclusion of finite amplitude effects in SWAN would require significant recoding.

Shoreline measurements are defined by first calculating the across-shore (x) position of the zero-crossing of total water depth, at each alongshore (y) grid point in the numerical model. These x positions are then interpolated to the y locations of the observational data. That is, shoreline observations are treated as observations of the shoreline position x_0 at a given y_0. Note this observation is nearly linear with respect to depth, provided the beach is approximately planar in the vicinity of the shoreline.

3.6. Observation Error Covariance, C_d

The main diagonal of C_d corresponds to the estimated error variances for the observations, which are provided as part of the remote sensing data extraction (see section 2). However, the data have been derived from overlapping spatial analysis windows, which implies observation errors are spatially correlated (i.e., C_d should also include off-diagonal terms). This is modeled by treating C_d as block-diagonal, with each block representing a particular data product (errors between different data products are assumed uncorrelated), where the ith block (representing one data product) is given by:

$$C_{di}(\Delta x,\Delta y)=w\Sigma_i\exp\left[-\left(\frac{\Delta x^2}{l_{xi}^2}+\frac{\Delta y^2}{l_{yi}^2}\right)\right]\Sigma_i^T+(1-w)\Sigma_i\Sigma_i^T, \tag{5}$$

where Δx and Δy are the separation between observations, l_{xi} and l_{yi} are set equal to $1/\sqrt{3}$ times the analysis window half-widths in the x and y directions, listed in Table 1, $\sum_i$ is a diagonal matrix containing the observation error standard deviations, and $w=0.9$ is a weighting factor. Additionally, errors in EO-k (and

EM-k) are assumed uncorrelated between different frequency bands (see sections 2.3.3. and 2.5), as are errors in EO-v at different alongshore transects (see section 2.3.2).

The weighting factor w allows the estimate of C_d to be biased toward a diagonal matrix, which helps ensure C_d is well conditioned (even in cases where observation windows are heavily overlapping, which does occur in the present data set). The choice of w was also used as a rudimentary calibration parameter for C_d. With $w = 0$ (diagonal C_d), the ensemble spread (standard deviation) was strongly underestimated, and corrections to bathymetry were amplified, sometimes at the expense of accuracy; this is interpreted as overfitting the observations. With $w = 1$, C_d was not as well conditioned, and estimates of some bathymetric features were overly smeared-out. The choice $w = 0.9$ was a compromise between those two extremes.

3.7. Ensemble Resampling and Covariance Inflation

The bathymetric ensemble obtained from the update equation (3) forms the basis for a new background ensemble for the next assimilation time. However, recall there is a possibility of excluding ensemble members with unacceptable depth variations (e.g., large islands); similarly, in rare cases certain realizations induce numerical instability in the forward model and therefore must be excluded (this occurred for 0.13% of all realizations in the experiment of section 4.3). Over time, these restrictions could lead to unacceptable shrinking of the ensemble size. To avoid this, the bathymetry ensemble is resampled after each update, producing a new ensemble of $N = 200$ members with conserved sample mean and covariance. The resampling is calculated using code from the EnKF-Matlab package by P. Sakov (available at http://enkf.nersc.no/Code/EnKF-Matlab/enkf-matlab-0.30.tar.gz). This code computes the singular value decomposition of the ensemble, and then replaces the right singular vectors with an $N \times N$ random orthogonal matrix.

Lastly, before proceeding to the next observation time, the spread of the ensemble is inflated using additive random noise. This accounts for errors due to time-evolution of bathymetry due to sediment transport (which have so far been neglected), and is similar to the "process error" defined by *van Dongeren et al*. [2008] and *Holman et al*. [2013]. To implement this in the ensemble system, the background bathymetry ensemble for assimilation step n (equivalently, observation time n) is defined as:

$$h^{b,n} = h^{a,n-1} + \sqrt{Q'}\,\delta h, \tag{6}$$

where $h^{a,n-1}$ is the analyzed ensemble from the previous update step (equation (3)), δh is an ensemble of unit variance random perturbations drawn from equation (2) with $L_x = L_y = 100/\sqrt{3}$ m, and Q' is a spatially dependent variance envelope. The definition of Q' is primarily based on *Holman et al*. [2013], who defined the spatial variability of process error variance (spatial covariance was not considered) using the equation:

$$Q(x, H_{m0}) = \int_{t_{n-1}}^{t_n} C_Q H_{m0}^2 \exp\left[-\frac{(x-x_0)^2}{\sigma_x^2}\right] dt, \tag{7}$$

where x is the across-shore coordinate, $C_Q = 0.067\ \mathrm{d}^{-1}$, H_{m0} is offshore significant wave height (measured), $x_0 = 150$ m, and $\sigma_x = 100$ m (the values of x_0 and σ_x reflect the typical location of breaking waves at this particular beach). *Holman et al*. [2013] obtained this formula by analyzing observed variability from 36 near-daily bathymetric surveys collected over 39 days in 1997 at Duck.

In addition, thresholds are applied to Q such that the background ensemble spread (standard deviation) at step n will be within user-defined bounds σ_{min} and σ_{max}:

$$Q'(x,y) = \begin{cases} \sigma_{min}^2 - (\sigma_h^{a,n-1})^2 & , \quad Q + (\sigma_h^{a,n-1})^2 < \sigma_{min}^2 \\ Q & , \quad \sigma_{min}^2 \le Q + (\sigma_h^{a,n-1})^2 \le \sigma_{max}^2 \\ \sigma_{max}^2 - (\sigma_h^{a,n-1})^2 & , \quad Q + (\sigma_h^{a,n-1})^2 > \sigma_{max}^2 \end{cases} \tag{8}$$

The use of a lower bound, σ_{min}, follows the "conditional covariance inflation" methodology used for parameter estimation by *Aksoy et al*. [2006]. It is intended to prevent filter divergence, defined as the situation where the filter's predicted variance becomes much smaller than the actual error, resulting in the filter ignoring subsequent corrections from data. Hence, σ_{min} should be set equal to the minimum expected error

Table 2. Skill Statistics, Comparing 6 September and 15 September Raw Bathymetric Survey Data (Figures 9c and 9d, Respectively) to Estimates From Data-Denial Experiments Presented in Figure 13 (Labels (a)–(c) Are Following Figure 13), as Well as the Initial Estimate Before Data Assimilation ("Initial," Figure 9a) and the Estimate When Assimilating All Observational Data ("All," Figure 9b)[a]

	6 Sep. Survey				15 Sep. Survey			
	Region A		Region B		Region A		Region B	
Obs. Type	r^2	ϵ (cm)	r^2	ϵ (cm)	r^2	ϵ (cm)	r^2	ϵ (cm)
Initial	0.49	57	0.93	51	0.68	55	0.88	65
(a) Current	0.81	35	0.96	41	0.85	43	0.93	52
(b) Wave number	0.81	33	0.96	39	0.86	36	0.94	48
(c) Shoreline-only	0.74	53	0.95	45	0.81	59	0.93	53
All	0.86	27	0.97	38	0.86	36	0.94	49

[a]The statistic ϵ is defined as the root-mean-square difference between surveyed and estimated bathymetry, and r^2 is the squared correlation. Both statistics are computed over two regions: region "A" is the area spanned by the alongshore current and wave number observations (union of red and blue polygons in Figure 1); region "B" is the combined region spanned by all of the observations (union of all polygons in Figure 1).

of the bathymetry prediction, which depends on unknowns such as model/filter errors. In practice, σ_{min} must be tuned for a given beach using validation data. For instance, in the present case comparisons to the true bathymetry (see section 4 and Table 2) suggested $\sigma_{min} = 0.25$ m. This value is recommended for future applications at the same field site. The use of an upper bound, σ_{max}, is to avoid unbounded growth of ensemble spread in sparsely observed regions [*Hamill and Whitaker*, 2005]. This parameter did not significantly affect the present results, and it is included only for completeness. A value $\sigma_{max} = 0.75$ m was used, 50% larger than the initial background variance.

4. Results

4.1. Observational Data Examples and Verification

4.1.1. Alongshore Current (EO-v)

Figure 3a shows an example EO-v data product (alongshore component of red arrows) at a time with dense data coverage, overlaid on a time-mean optical image which illustrates the locations of wave breaking. For visualization purposes, the EO-v estimates have been smoothed to reduce the effects of noise, such that the across-shore component of current could be estimated from the continuity equation using measured

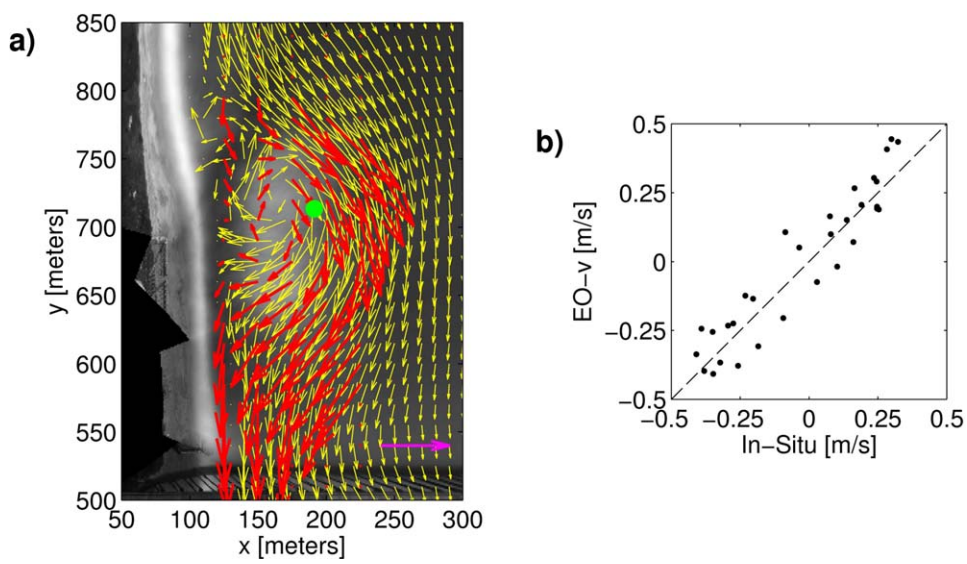

Figure 3. (a) Example data product from Optical Current Meter (EO-v): 13 September, 0830 EST. Red arrows represent spatially smoothed measured alongshore currents, with across-shore currents derived using continuity equation; yellow arrows are a numerical model prediction using measured bathymetry; magenta scale arrow in lower right represents 0.5 m/s; background is an Argus time-exposed image from the same time period. (b) Comparison between EO-v alongshore current, and in situ (location indicated by green dot in Figure 3a) measurements of depth-averaged current.

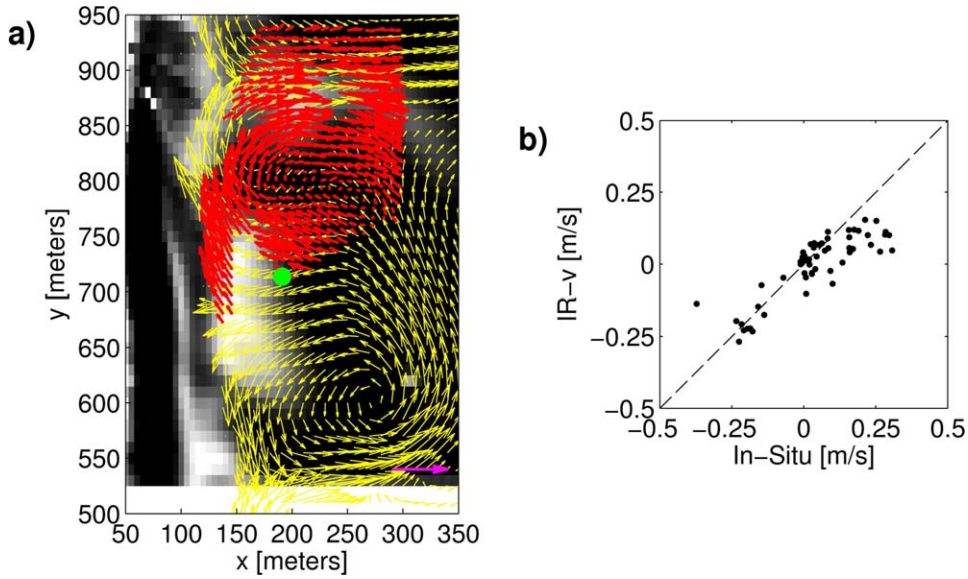

Figure 4. (a) Example data product for Infrared Particle Image Velocimetry: 13 September, 1800 EST. Red arrows represent measured currents; yellow arrows are a numerical model prediction using surveyed bathymetry; magenta scale arrow in lower right represents 0.5 m/s; background is a time-exposed radar backscatter image from the same period. (b) Comparison of IR-v estimates of alongshore current, and in situ (location indicated by green dot in Figure 4a) measurements of depth-averaged current.

water depths (this processing was not applied when assimilating the data, or when comparing to in situ observations below). Figure 3a also shows time-averaged predictions from the forward model (yellow arrows), using measured bathymetry from 15 September (linearly interpolated to the model grid, and spatially smoothed). This demonstrates the model could agree well with the remote sensing data, given accurate bathymetry. In this case, the model is correctly predicting a gyre-like flow caused by a gap in the nearshore sandbar. This type of circulation was common during the experiment, and mainly occurred during low tide [*Haller et al.*, 2013].

Figure 3b shows a comparison between EO-v data and depth-averaged currents measured at $(x, y) = (191, 714)$ m (nominal depth 1.5 m). The data shown cover the period 11–14 September (EO-v collections began 11 September, and in situ collection ended 14 September), excluding an 8.5 h period during rain on 12 September. To make this comparison, quality-controlled EO-v observations were averaged within a radius of 20 m around the in situ gage, excluding cases with fewer than five such observations; 31 EO-v collections passed this criteria. The in situ data were then time-averaged over the EO-v collection windows. Although the data set is small, the results indicate good skill for the EO-v measurements: root-mean-square (rms) error was 9.3 cm/s, and $r^2 = 0.88$, comparable to the verification results of CHF.

4.1.2. Alongshore Current (IR-v)

An example IR-v result is shown in Figure 4a, similar to Figure 3a. Again, the forward model agrees qualitatively well with the remote sensing data, in a case where bathymetry is accurately known (15 September survey).

The IR-v data also compare well with in situ observations, as shown in Figure 4b (using the same in situ data set and method of comparison as described above for the EO-v data, Figure 3b). In this case, the comparison spanned 9–14 September, and included 63 IR-v collections. Root-mean-square error for the IR-v data was 8.9 cm/s, and $r^2 = 0.71$.

4.1.3. Wave Celerity (EO-k and EM-k)

EO-k and EM-k data were validated using a comparison to wave number data from in situ pressure gage measurements. The in situ data consist of 34 min 2 Hz time series, collected hourly, at locations $(x, y) = (233, 940)$, (375, 939) and (446,938) m (see Figure 1). Cross-spectral analysis between adjacent pairs of instruments was used to estimate the across-shore component of wave number in each remote sensing frequency band. Corresponding estimates from EO-k and EM-k (taking wave angle into account using the corresponding estimates of wave angle) were extracted by interpolating to the midpoints between gage

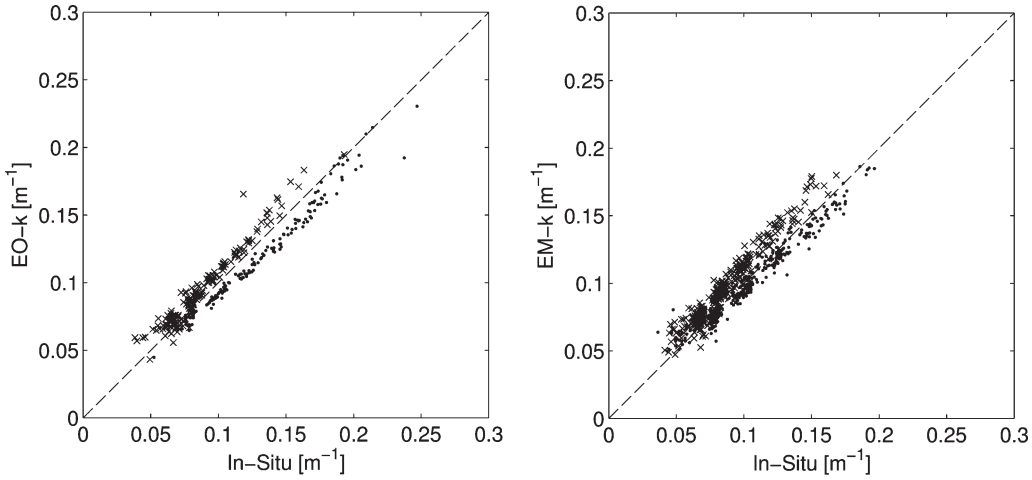

Figure 5. Radial wave number from (left) EO-k and (right) EM-k, compared to an estimate from cross-spectral analysis of in situ pressure gage pairs. Dots represent in situ gage pair $(x, y) = (233, 940)$, (375, 939) m; crosses represent (375,939), (446,938) m.

pairs. Figure 5 shows the resulting comparison, for 75 EO-k data collections covering the time period 9–17 September (left-hand plot) and for 121 EM-k collections spanning 10–17 September (right-hand plot). The agreement is good, with overall rms error 0.011 m^{-1} and $r^2 = 0.93$ for EO-k, and 0.010 m^{-1} and 0.89 for EM-k. Much of the error is due to an apparent bias between the in situ and remote sensing estimates, which could be explained by reasonable synchronization offsets among the in situ instrument clocks (1–2 s; K. Hathaway, personal communication). If this bias was removed, skill increased to rms-error 0.0060 m^{-1} and $r^2 = 0.97$ for EO-k, and 0.0065 m^{-1} and 0.95 for EM-k.

Direct comparison of the radar and optical-based wave number products also showed good agreement for the most part. However, there was a systematic bias toward smaller measurements of wave number by EM-k, in a nearshore region roughly equal to the extent of the surf zone. To resolve this discrepancy, it was decided to disregard radar data (hence rely solely on the optical data) in the region $x < 250$ m. This is justified by the fact the optical data has superior pixel resolution nearshore; note as waves enter shallow water their wavelength becomes small, making pixel resolution increasingly important.

4.1.4. Shoreline Identification (EO-xs)

An example EO-xs data product is shown in Figure 6. Note the shoreward maximum of variance (red line) corresponds to the edge of the shorebreak, and is used to represent the shoreline. Shoreline observations were validated using a visual check against optical imagery, and manual intervention was applied when needed.

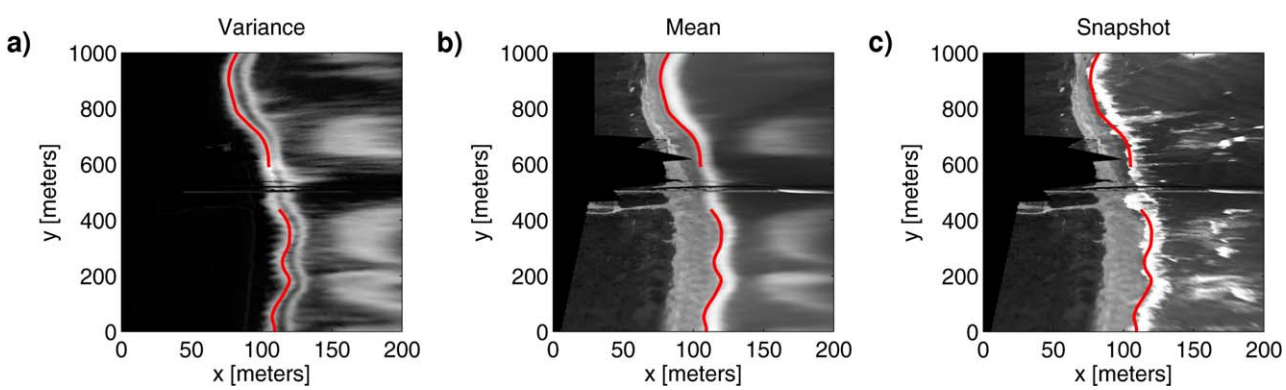

Figure 6. Example shoreline from optical imagery on 13 September, 1200 EST. (a) Pixel variance image, with location of shoreline (shoremost local maximum of variance) indicated by red line; (b) mean pixel intensity, and (c) example snapshot, are also shown for visual reference. Note axis aspect ratio is nonunity to emphasize alongshore variability in the shoreline.

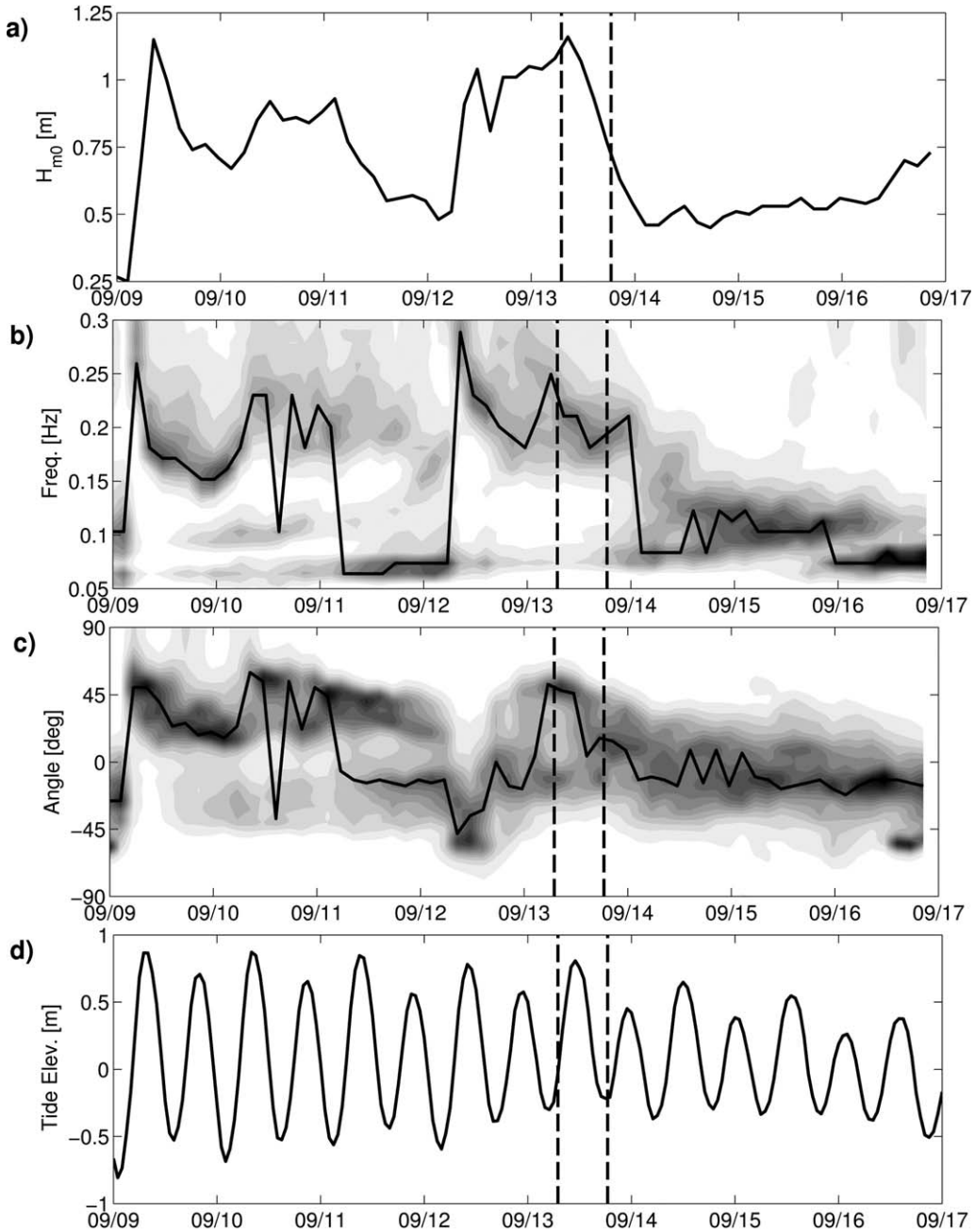

Figure 7. Conditions observed during experiment versus time in EST. The start/end time of the 13 September test case presented in section 4 is marked by vertical lines. (a)–(c) Observed wave conditions in 8 m depth: significant wave height H_{m0}, and integrated frequency and directional wave energy density (shown as shading in Figures 7b and 7c, normalized to unit energy for each time), with peak frequency and direction marked by solid lines. Wave directions are measured counterclockwise from the positive—*x* axis to the direction waves are coming from. (d) Observed tidal elevations relative to the NAVD88 vertical datum.

4.2. Data Assimilation Experiment Setup

Conditions observed during the experiment, including wave height, frequency/directional distribution, and tidal elevation, are shown in Figure 7. Two wave events exceeding 0.75 m significant wave height were observed during the experiment. During these events wave frequencies were near 5 s, and a broad range of wave incidence angles was observed.

Figure 8 shows the number of quality-passed data points for each remote sensing data product, where each point in the plot represents a single 1/2 h observation cycle. At certain times, some sensors were able

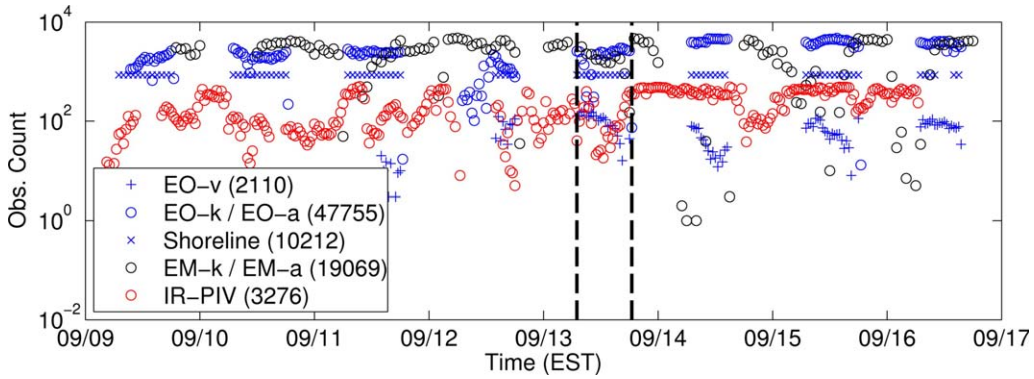

Figure 8. Number of remote sensing observation data points versus time in EST. The start/end time of the 13 September test case presented in section 4 is marked by vertical lines. Legend indicates the type of observation; the total number of observations during the 13 September test period is listed in parentheses.

to collect more data than others (e.g., EO-based products are not available at night). Also note the first of the two wave events (9–11 September) occurred before the collection of EO-v data (blue crosses).

The assimilation system will be demonstrated using an 11.5 h period during daylight hours (0700–1830 EST) on 13 September, spanning nearly a full tidal cycle during the second wave event mentioned above. This time period is marked by vertical lines in Figures 7 and 8. It was important to include a wave event in the test, in order to test assimilation of nontrivial wave-induced currents. This particular event also had high collection rates in all remote sensing data products (see Figure 8), which allowed for an intercomparison between assimilation of different data (section 4.5). Other time periods and longer assimilation windows were tested, and generally gave similar results (although, see section 5.1, for an exception).

As shown in Figure 7, combined significant wave height during the test case varied from 0.7 to 1.1 m. Wave spectra were somewhat complex, consisting of at least two sea components and a weaker swell component. The observed dynamics were spatially nonuniform, primarily due to the presence of nonuniform bathymetric features (see surveyed bathymetry in Figures 9c and 9d). Most notably, a rip current was observed during low tide at $y \approx 750$–950 m, apparently due to a gap in the nearshore bar/terrace which caused a nonuniform wave breaking pattern. This rip current is of particular interest, because it was in the field of view of all of the remote sensing instruments. For instance, it can be seen in the example data shown in Figures 3a and 4a.

4.3. Estimated Bathymetry

The data assimilation system was initialized using a background bathymetry based on 29 years of bathymetric surveys (253 surveys in total), which was merged/interpolated to the model grid using a linear Loess interpolator [*Plant et al.*, 2002] having length scales of $l_x = 20$ m and $l_y = 200$ m (resulting in a high degree of smoothing). The result is shown in Figure 9a. Uncertainty for this background bathymetry, C_h, was initialized as described in section 3.3, using $L_x = L_y = 100/\sqrt{3}$m, and $\sigma_h = 0.5$ m. This choice of L_x is consistent with values estimated from the sample covariance of the 253 historical surveys, for the inner-bar region of $100 < x < 400$ m (whereas beyond $x = 400$ m the historical L_x becomes larger, of order 150 m). The historical alongshore correlations are more complex, and are not well modeled by equation (2), mainly due to the influence of the FRF pier. In general, however, such alongshore covariance information would not be known a priori, and instead an isotropic covariance matrix is used here for simplicity.

Note the imposed initial background estimate includes very little information pertaining to the actual bathymetry during the experiment. The prior-mean contains only the approximate across-shore beach shape, and mild scour under the FRF pier. And the presumed length scales are homogeneous and isotropic, without assumptions regarding the typical bathymetric features at this beach. This ensures any subsequent corrections to bathymetry can be clearly attributed to information in the assimilated data, rather than user-specified prior knowledge. Also note the spatially dense nature of the assimilated data means the background covariance is not relied upon to spatially "extrapolate" corrections to bathymetry [cf. *Wilson et al.*, 2010]. Instead, the imposed length scales L_x and L_y primarily dictate the spatial smoothness of the result.

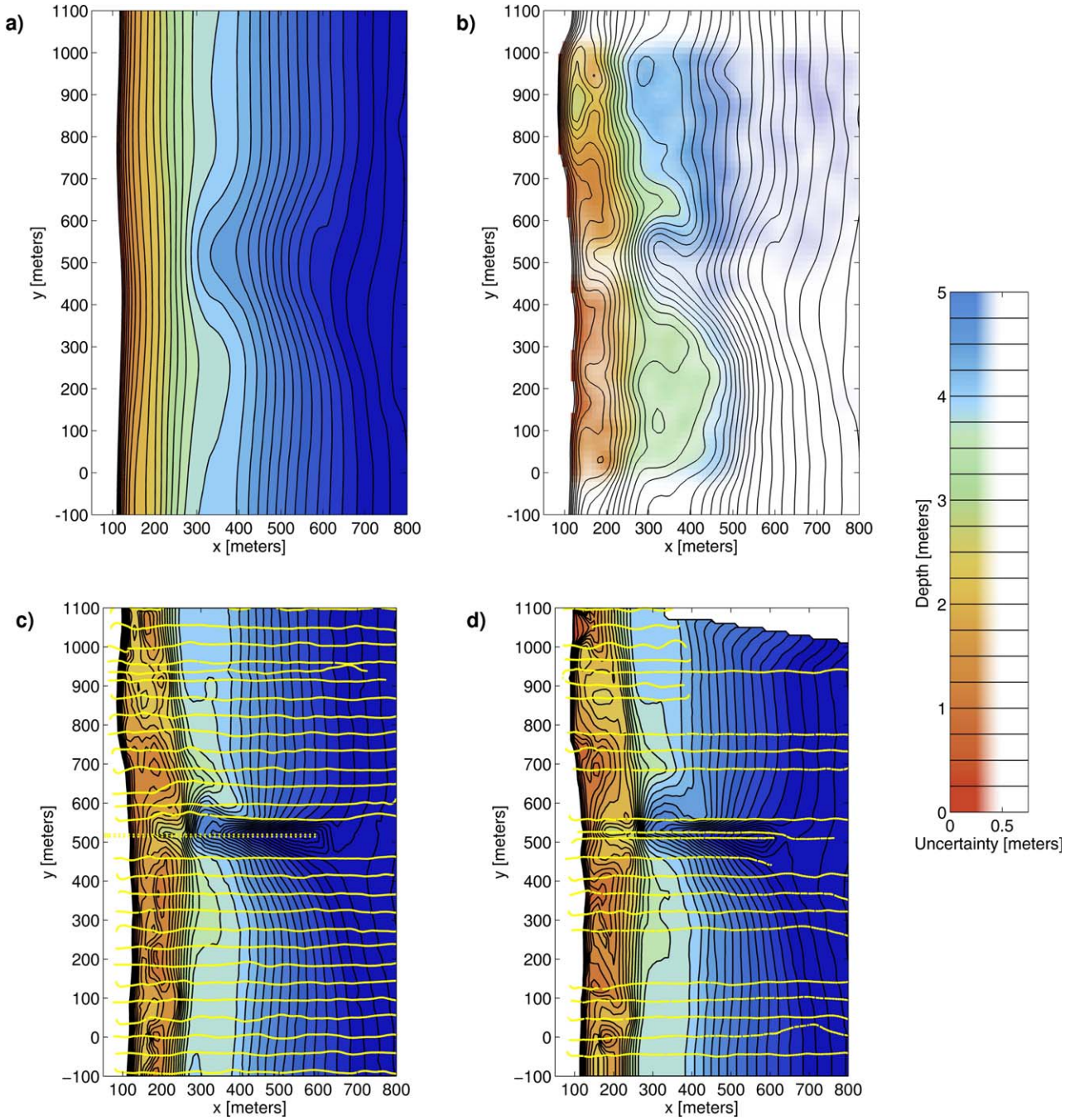

Figure 9. (a) Background bathymetry h^b used to initialize the ensemble assimilation system: a climatological average of bathymetry observed at the field site. (b) Updated bathymetry after assimilating all observations, over 24 assimilation cycles (ending 1830 EST). (c and d) Surveyed bathymetry from (c) 6 September to (d) 15 September, where individual survey data points are plotted as yellow dots, and interpolated/smoothed depths are shown as colors (white area in top-right of 15 September bathymetry is due to a gap in the data). Colorbar with contour marks at far right applies for all plots, and refers to depth relative to the NAVD88 vertical datum; in the case of the updated bathymetry (Figure 7b), the same colors and contours at are used, but color transparency is scaled to represent the posterior estimate of bathymetric uncertainty.

Limited tests with different length scales (e.g., $L_x = 50$ m, $L_y = 100$ m) gave similar results but with less smoothing. In general, the desired amount of smoothing will depend on the density of the observational data, and the intended application for the bathymetry [*Plant et al.*, 2009].

Figure 9b shows the estimated bathymetry after assimilating the 11.5 h test data set (24 observational data cycles). Uncertainty is represented using color transparency (see colorbar legend), which shows that areas

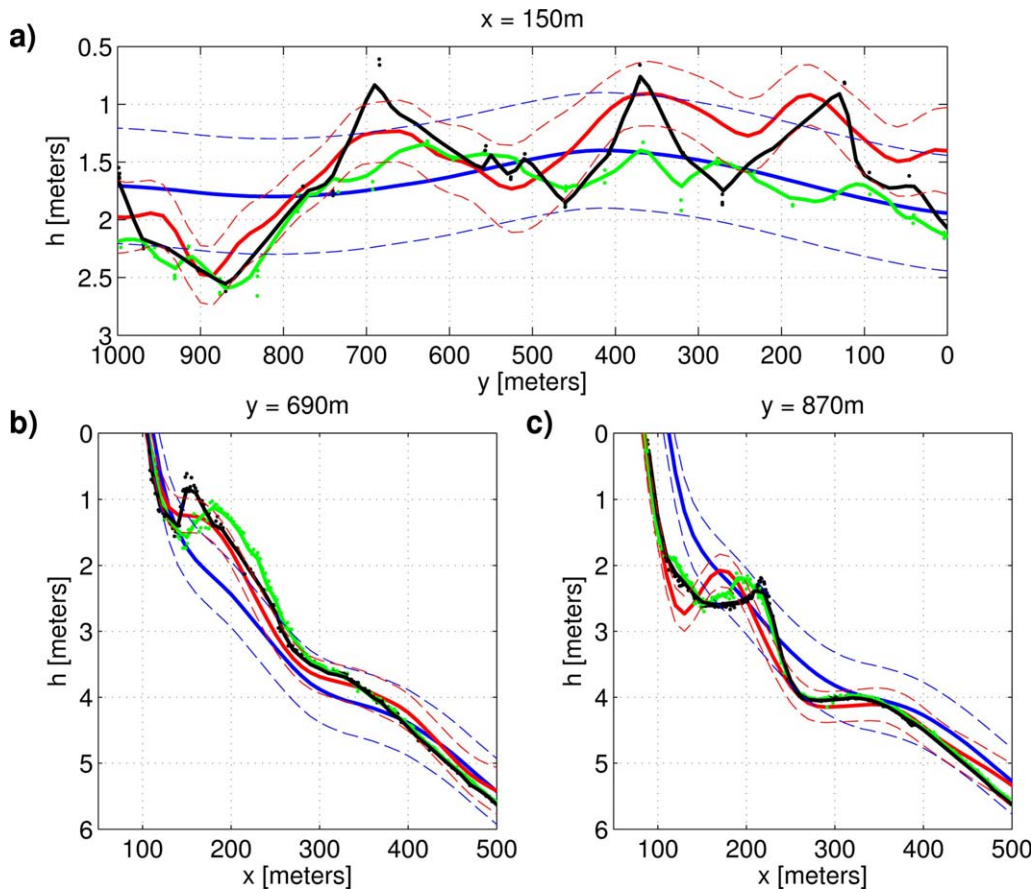

Figure 10. Transects from initial (blue) and final (red) estimated bathymetry (as in Figures 9a and 9b, respectively), and ± one standard deviation (dashed lines), compared to measured bathymetry on 6 September (green) and 15 September (black). (a) Alongshore transect is from $x = 150$ m, located over the nearshore terrace; (b and c) across-shore transects are from $y = 690$, 870 m. Dots represent measured data from within 2 m of the alongshore transect in Figure 10a, and within 10 m of the across-shore transects in Figures 10b and 10c; green and black lines represent smoothed 2-D interpolation of raw survey data, as in Figures 9c and 9d.

having fewer available measurements (cf. Figure 1) correspond to larger uncertainty in the posterior estimate, as expected.

The accuracy of the estimated bathymetry can be assessed qualitatively by comparing to the survey data in Figures 9c and 9d. These shows a nearshore bar at $x \approx 200$ m, which migrated onshore over time to form a more terrace-like nearshore feature. The bar/terrace was also incised with several channels ($y \approx 100$, 250, 900 m) which caused alongshore nonuniform wave breaking patterns. There was also a prominent trench at $y \approx 500$ m, which is a persistent feature at this site due to scour around the FRF pier pilings. While none of these qualitative features existed in the initial background bathymetry (Figure 9a), all are fairly well represented in the final estimated bathymetry (Figure 9b). This is further illustrated using individual across-shore and alongshore transects in Figure 10. A transect of the estimated bathymetry over the nearshore bar/terrace (red line in Figure 10a) shows that assimilation of data correctly captures the location and approximate amplitude of rip channels, in good agreement with the survey data from 15 September (black line). An across-shore transect at $y = 690$ m shows that the across-shore profile of the nearshore bar/terrace is also fairly well captured, as is a secondary terrace at $x \approx 350$ m; another across-shore profile at $y = 870$ m also shows good agreement, including a corrected shoreline location, although in that case the inner bar/terrace was poorly estimated.

Figure 11 shows differences between the raw survey data and the estimates of bathymetry before and after data assimilation. Positive values in this plot represent overestimates of depth. Despite ambiguity as to which survey should represent the "truth" for 13 September, both surveys indicate the bathymetry estimate is generally improved by the assimilation of data. For example, the initial estimate did not include a bar/

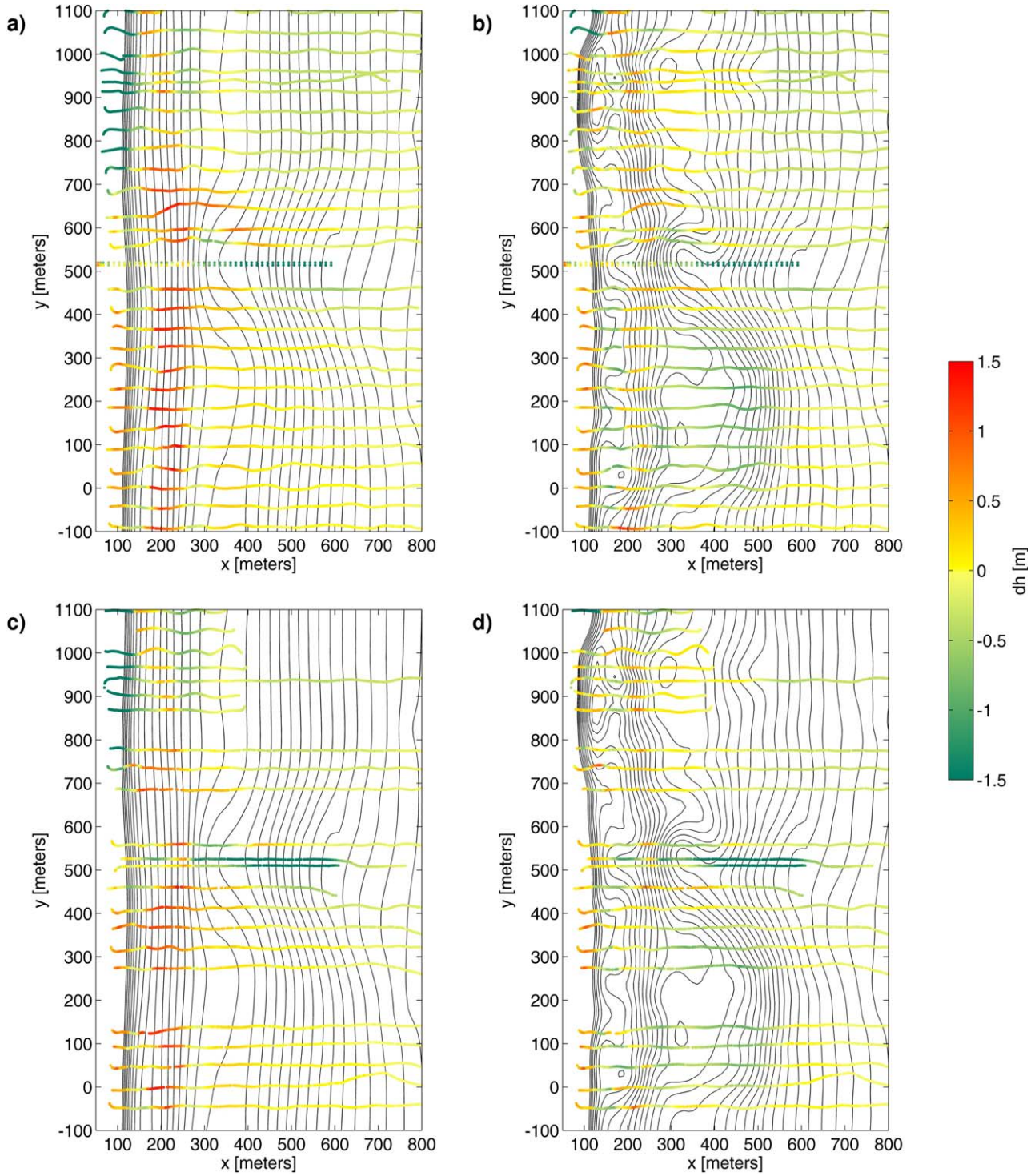

Figure 11. Difference between estimated bathymetry and raw bathymetric survey data. (a and b) Use data from the 6 September survey, showing differences (a) before and (b) after data assimilation; (c and d) are the same, but using data from the 15 September survey. Positive differences indicate an overestimate of depth. Black contours are the estimated depths as in Figure 9.

terrace, resulting in the initial bathymetry being overly deep for approximately $150 < x < 250$ m, an error which was largely corrected by data assimilation.

A region of low skill, on the other hand, occurred in the south part of the domain offshore of the surf zone, roughly $0 < y < 400$ m and $250 < x < 500$ m, where the system estimated overly shallow depths. Note only

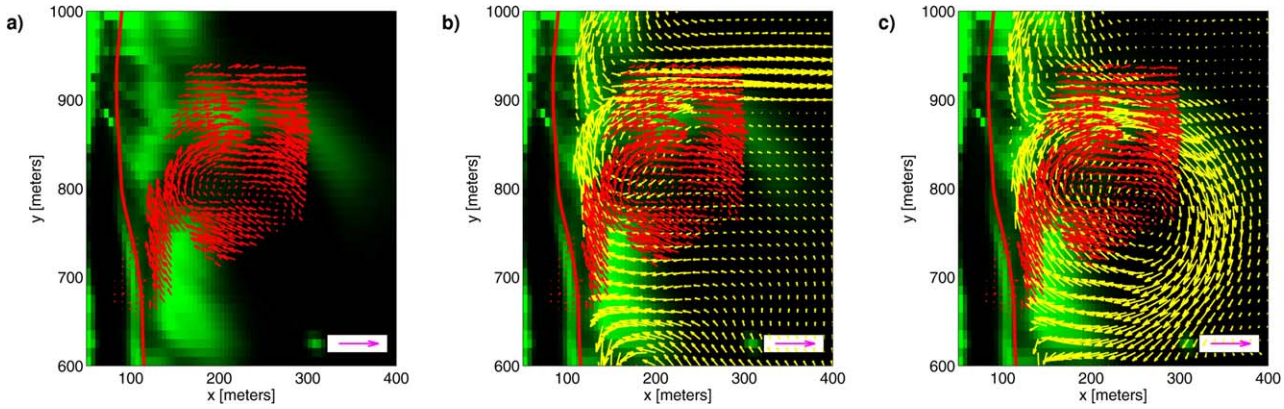

Figure 12. Measurements and forward model predictions for 13 September, 1800 EST (low tide). Background shading represents X-band radar backscatter averaged over a 17 min collection period; high backscatter (green) corresponds to breaking waves, and/or surface roughness due to the presence of a rip current [*Haller et al.*, 2013]. Red arrows are IR-v measurements of currents (scale arrow in bottom-right is 50 cm/s), which confirm the presence of a rip current at $y \approx 900$ m. Red line is optical-based shoreline position. Yellow arrows are predicted time-averaged currents from a forward model run using (b) the estimated bathymetry after assimilation of data from 0700–1200 EST, and (c) the estimated bathymetry after assimilation of data up to and including 1800 EST.

one observation type, wave number, was assimilated in this region (see Figure 1). Inspection of the data showed EO-k measured wave celerities were indeed consistent with such shallow depths (based on linear wave dispersion), and the alternative data assimilation method of cBathy Phases 2–3 [*Holman et al.*, 2013] produced similar results. EM-k data were sparse in this region, but the few data points that were available showed larger wave celerity than measured by EO-k (i.e., consistent with larger depths). Hence, low skill in this region is likely due to an isolated problem with observational (EO-k) data quality, not with the data assimilation method.

Although Figure 9 only presents the final bathymetry estimate at the end of the 11.5 h test case, much of the correction occurred rapidly, within the first few hours. Depending on how skill was assessed (see Table 2), approximately 90% of the improvement in accuracy was achieved after 1–4.5 h. Afterward, skill was relatively constant with only minor additional adjustments to bathymetry. This suggests the system would be tolerant to gaps or patchiness in data (e.g., due to brief rain or fog periods), because it would recover rapidly once new data became available. It also suggests the possible use of the system for resolving rapid changes in bathymetry through time, although this has not been proven in the present test where bathymetry did not change rapidly.

4.4. Improved Prediction of Currents

After assimilating data and correcting bathymetry, the forward model also achieved increased skill in predicting surf zone currents. This will be demonstrated using a rip current which appeared during low tides, at $y \approx 900$ m, coincident with a gap in the nearshore bar/terrace. This rip, which occurred on multiple days, was well imaged by time-averaged radar backscatter imagery [*Haller et al.*, 2013], and was also detected by IR-v measurements.

During the data assimilation experiment, observations indicated the presence of a weak recirculating rip current at $y \approx 800$ m arly in the day, from 0700 EST until approximately 0900 EST (e.g., Figure 3a). This was followed by a long period in which no rip current was observed, approximately 0900–1200 EST. By 1500 EST a prominent rip current had developed at $y \approx 900$ m and persisted until after 1830 EST.

To test the forecasting ability of the system, data were assimilated in the time period 0700–1200 EST, then the model was run forward without assimilating data to predict currents at low tide, 1800 EST. The reason 1200 EST was chosen as a cutoff was that near that time a reversal of currents was observed at $y \approx 700$ m, a precursor to the formation of the rip current; in other words, the onset of the second rip current (the forecast "target") was not included in the assimilated data.

Figure 12 shows the resulting prediction of currents at 1800 EST. By assimilating the 0700–1200 EST data, the model was capable of predicting the rip current in roughly the correct location (Figure 12b). If no data were assimilated, the bathymetry remained nearly alongshore uniform (i.e., as in Figure 9a), and no rip

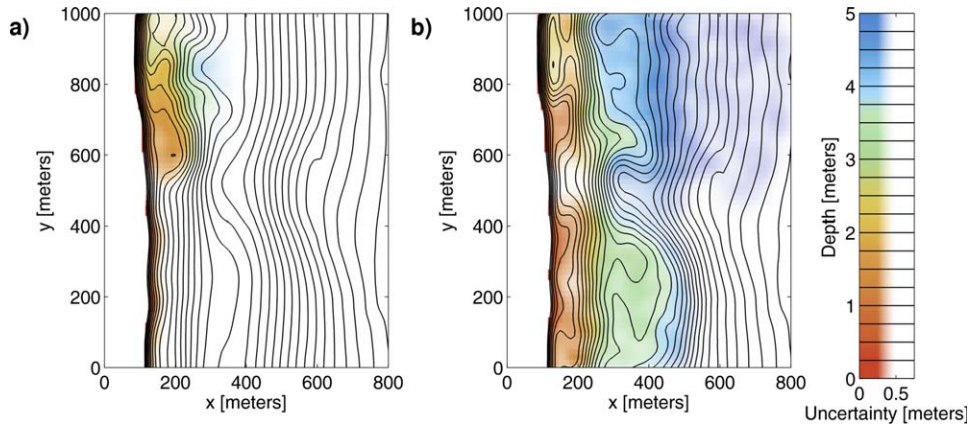

Figure 13. Estimated bathymetry from data-denial experiments (see text), plotted as in Figure 9b. Each result is from assimilating EO-xs observations and one other observation type: (a) alongshore currents (EO-v and IR-v) and (b) wave number (EO-k and EM-k).

current was predicted (not shown). Hence, assimilation of data resulted in the prediction of a bathymetry-controlled rip current, without the use of any direct bathymetry observations. An even more accurate prediction was obtained if data were also assimilated during 1200–1800 EST (Figure 12c).

Note the forward model is not expected to accurately predict the trajectory of the rip current once it exits the surf zone (roughly $x > 200$ m in this case), regardless of the accuracy of bathymetry. In that region, there is likely to be a strong influence from wave-current interaction [*Haas et al*., 1998; *Yu and Slinn*, 2003] as well as 3-D aspects of circulation [*Haas and Svendsen*, 2002], both of which have been neglected. The prediction of the trajectory in Figure 12c appears accurate, but was found to be sensitive to small details in the bathymetry (e.g., when using the measured bathymetry, Figure 4) and so may simply have been a coincidence. On the other hand, the ability to predict the location of the rip inside the surf zone (after assimilating data) is within the expected capabilities of the model, and was a robust result.

4.5. Observation Impact and Quantitative Skill Assessment

To judge the impact of each individual observation type on the estimated bathymetry, a series of data-denial experiments were conducted, in which only one observation type was used in addition to shoreline observations. The reason shoreline observations were always included was that the initialized shoreline (i.e., from the climatological average bathymetry, Figure 9a) was further offshore than the true shoreline; if the shoreline location was not corrected, many observations fell on "dry land" in the model and hence could not be assimilated.

Figure 13 shows the final bathymetry estimate (after 24 assimilation cycles) for each observation type, including a case where only shoreline data were assimilated. Assimilation of data generally produced qualitative improvement in the bathymetry estimate in the region where observations were available (see Figure 1). In areas where there were no observations, assimilation has less of an effect and the estimated uncertainty is large.

Table 2 presents skill statistics for the bathymetry estimates from the various data-denial experiments presented in Figure 13, as well as for the full assimilation test, Figure 9b, and the case with no assimilation, Figure 9a. Skill is assessed by comparison to raw data from each of the bathymetric surveys (Figures 9c and 9d), for two different subregions: (A) the region where both wave and current observations were available (i.e., union of red and blue polygons in Figure 1), and (B) the combined region spanned by all of the observations (nearly the entire model domain). Note differences in statistics using the 6 September data versus the 13 September data were found to be due to changes in sampling distribution (cf. Figure 11), and hence should not be intercompared.

In both surveys, the statistics consistently show that assimilation of either wave number or alongshore current produced a quantitative improvement in bathymetric accuracy, relative to the initial estimate with no

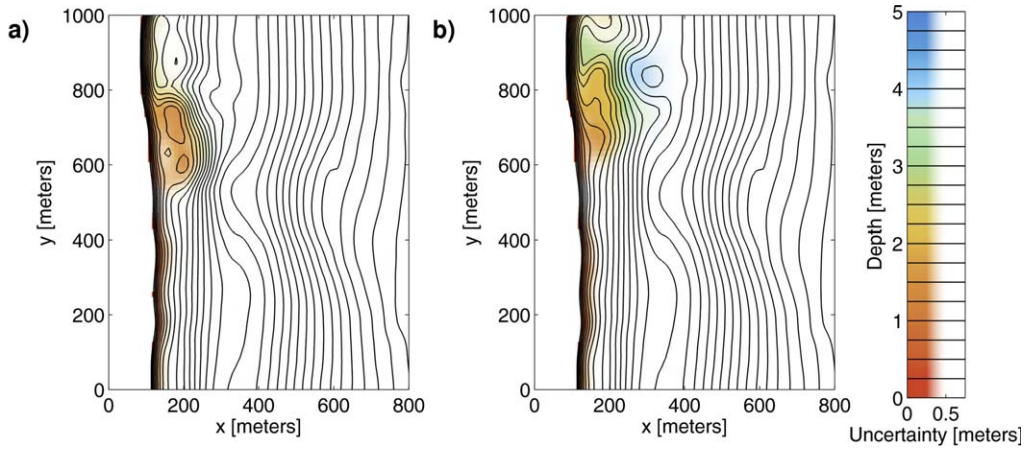

Figure 14. As in Figure 13, but assimilating shoreline plus (a) EO-v currents, and (b) IR-v currents. Note the different observational footprint of the two products, and the resulting differences in estimated bathymetry.

assimilation. Wave number observations produced a more accurate estimate than did alongshore current observations, which can be attributed to two factors. First, the relationship between wave number and bathymetry is more clear-cut, via the wave dispersion relationship (equation (4)). Second, the density of wave number observations far exceeded that of currents (see Figure 8); this is because waves are nearly always visible in the remote sensing imagery, and can be analyzed at multiple frequencies for each location, whereas observations of currents rely on tracking of ephemeral image features.

Another data-denial experiment involves the effect of spatial coverage on the estimation of bathymetry from alongshore currents: Figure 14 compares the results when assimilating EO-v currents versus IR-v currents (again, in addition to shoreline data). In this comparison, note the observed region coincides with the region presented in Figure 12, where a gap in the nearshore bar/terrace caused a rip current to occur. It happened that the IR-v data coverage was largely over the gap itself, whereas the EO-v data was concentrated slightly to the south, over the bar/terrace. Hence in the case where only the IR-v data were assimilated (Figure 14b) the assimilation system would have had fewer observations over the bar/terrace. In that situation, the system apparently obtained a fit to the observations by creating a deep channel at $y \approx 900$ m. The EO-v assimilation run, on the other hand, obtained a fit to observations by creating a "bump" at $y \approx 700$ m (Figure 14a), where data were readily available. If both EO-v and IR-v were assimilated together (Figure 13a) the estimate included both the bump and a more-realistic channel, essentially an average of the two individual results. Surprisingly, despite their differences all three of these bathymetry estimates resulted in the prediction of a low-tide rip current at $y \approx 900$ m, similar to Figure 12. This illustrates the complex and indirect relationship between bathymetry and currents, and underscores the importance of data coverage when attempting to invert that relationship.

5. Discussion

5.1. Effects of Model Error

As shown in Figures 3a and 4a, the forward model is capable of predicting surf zone flows with a high degree of accuracy. Still, an important consideration in the application of the assimilation system is the potential for unaccounted-for errors in the forward model. Only bathymetry error has been considered here, whereas model physics and boundary conditions have been assumed perfect. However, this is not always the case. One exception occurred during high tide on 11 September, at which time a 30–40 cm/s alongshore current was observed in the in situ and remote sensing data, despite minimal wave breaking and wind (winds on this day were less than 5 m/s). This current was observed even in 8 m depth, and was presumably caused by larger-scale processes [*Lentz et al.*, 1999], which are not included in the model. When alongshore current observations were assimilated in this case, the system obtained a fit to the observations by producing a spurious nearshore bar. This error persisted until later that day, when waves heights increased and offshore currents weakened, such that nearshore currents were once again driven by wind

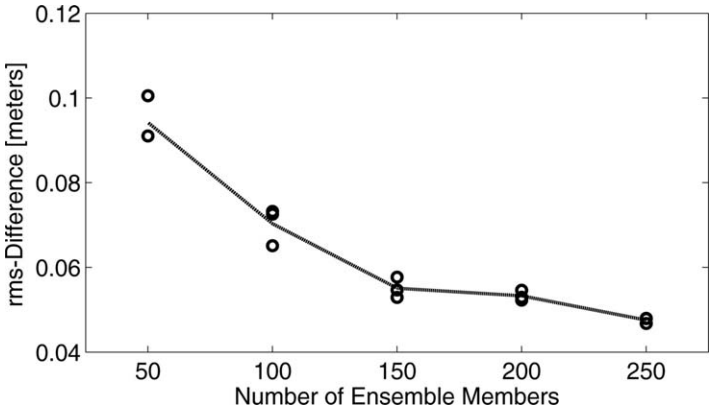

Figure 15. Root-mean-square difference in estimated bathymetry for various ensemble sizes in a simplified assimilation system (see text), compared to a reference run with 300 ensemble members. In each case, differences are computed over the domain $50 < x < 500$ m and $0 < y < 1000$ m, and over each of the 24 assimilation cycles. Three realizations (indicated by circles) were performed for each ensemble size, to account for differences due to the stochastic nature of the filter. Note, the rms difference computed for two runs with 300 ensemble members each was 4.8 cm, which defines an approximate "noise floor" for the statistic.

and wave-induced forcing as assumed by the model. With the model error thus reduced, the system gradually recorrected the spurious nearshore bar and regained skill by 12 September.

Another potentially important source of model error is due to offshore wave boundary conditions. At Duck, model boundary conditions can be specified using in situ observations of frequency-directional wave spectra from a highly accurate (and unique) observational array. At other sites, boundary conditions would be derived from larger-scale wave forecasts, which likely have more error. An interesting avenue for future work would be the development of a data assimilation system which corrects for both bathymetric error (as in the present work) and boundary condition error. *Veeramony et al*. [2010] have studied the latter problem, correcting boundary condition errors in a nearshore wave model using data assimilation.

5.2. Representation of Posterior Uncertainty

The present results showed a tendency toward underprediction of posterior uncertainty (as compared to errors based on bathymetric survey data), similar to the results reported by *Holman et al*. [2013]. This motivated the use of conditional additive inflation of the ensemble spread (section 3.7), which was generally applied in regions nearshore with dense observational data coverage. In other words, the estimated bathymetric uncertainty in such regions was held close or equal to the specified minimum value of 0.25 m (after about five observation cycles), and in that sense it was not truly "dynamically" updated over time. This can be seen in Figures 9b and 13, where uncertainties are generally close to 0.25 m in regions where there was dense observational coverage.

The need for conditional inflation may be attributed to several factors. First, errors in the forward model have been neglected (see section 5.1); if model errors do exist, neglecting them would tend to cause underprediction of uncertainty [*Houtekamer et al*., 2008]. Second, there is the possibility of misspecification of observational error covariance. Inclusion of spatial correlation in equation (5) (section 3.6) reduced the tendency to underpredict bathymetric uncertainty, but did not fix the problem completely.

Further improvements are therefore recommended to reduce the underprediction of uncertainty. This would include refining the method used for covariance inflation, adding a systematic representation of model error, and improving the specification of observational error covariance. The methods used here (see sections 3.6 and 3.7) are a first attempt, but more sophisticated methods do exist [e.g., *Dee*, 1995; Houtekamer *et al*., 2008; *Li et al*., 2009].

5.3. Ensemble Size

To assess the effect of ensemble size in a simplified (computationally cheap) setting, a simplified system was defined in which wave height is represented by a single deterministic SWAN model run (assuming zero current) in equation (4). This eliminated the need for an ensemble of wave (SWAN) and circulation (ROMS) model runs, and hence greatly reduced runtime, at the expense of not being able to assimilate velocity observations (similar to the method of *Holman et al*. [2013]). The simplified system was applied to the test case described in section 4.3, assimilating EO-k and EO-xs observations. Figure 15 shows the convergence of estimated bathymetry (with respect to ensemble size) from the simplified system, by comparing results

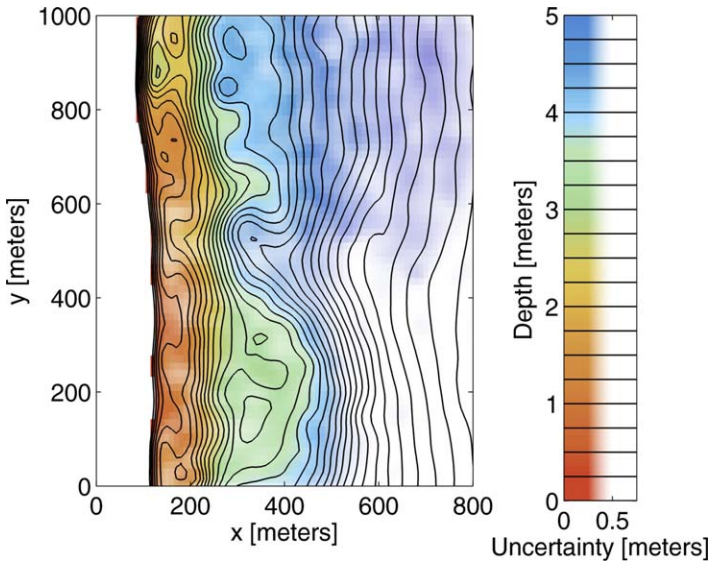

Figure 16. Bathymetry estimate as in Figure 9b, but using 1/4 ensemble size (50 members rather than 200).

with increasingly large ensemble sizes to a 300 member reference run which also used the simplified system. Even for the smallest ensemble size tested, 50 members, the effect on the bathymetry estimate is not excessive (order 10 cm). In fact, the estimated bathymetry was not qualitatively different for any of the ensemble sizes tested. With that in mind, a 50 member ensemble run was tested using the full system and all available data. The result is shown in Figure 16, which should be compared to the 200 member result shown in Figure 9b. The 50 member estimate still includes basic bathymetric features, although it appears to be prone to error at short length scales. When compared against bathymetric survey data, the quantitative skill of the 50 member estimate is nearly identical to the 200 member estimate (differences of less than 2 cm in root-mean-square error, and less than 0.01 in squared-correlation, based on statistics listed in last row of Table 2).

6. Conclusions

The present work demonstrated a new application of the ensemble Kalman filter (EnKF) to the problem of surf zone bathymetric uncertainty. The method was applied to a test case spanning 11.5 h of remote sensing observations collected at Duck, NC. Assimilation of wavefield observations (frequency-wave number pairs, i.e., wave celerity), circulation observations (alongshore current), and shoreline observations all led to an improved estimate of bathymetry. After assimilating only 5 h of data, the model became capable of predicting an observed surf zone rip current, without the use of any in situ bathymetry observations.

An important feature of the EnKF method is the ease with which it can be extended for assimilation of new geophysical data types, and for new physical processes in the forward model, without the need to redefine the assimilation system itself. This contrasts with existing methods such as that of *van Dongeren et al*. [2008], who relied on explicit knowledge of the derivative of the observable with respect to depth (effectively, an adjoint model), or *Holman et al*. [2013], who converted the observations to depth estimates prior to assimilation. The EnKF has no such requirements, which is beneficial when incorporating/testing the assimilation of new and novel observation types such as remotely sensed time-averaged currents. The ability of this method to assimilate currents may be a particular advantage in environments where observation coverage varies between different observation types. An example would be a coastal inlet, where wavefield observations would dominate nearshore, but observations of currents would dominate within the inlet itself.

In the present experiment, frequency-wave number observations were available in high density over a broad field of view, and those observations were most successful for estimating bathymetry. Assimilation of alongshore current observations was also successful, although there was evidence that the bathymetry was not uniquely determined unless the data had good spatial coverage.

Section 4.4 showed that after assimilating remote sensing data to correct bathymetry, the forward model became capable of predicting a rip current. This suggests a potential for making surf zone forecasts without the use of any in situ observations. A remaining barrier to such an application would be the influence of

errors in model boundary conditions, in particular the accurate specification of waves at the offshore boundary.

Acknowledgments
This work was funded under ONR grants N00014-10-1-0932 and N00014-07-1–0852. We wish to thank the field crews and technicians who assisted with the collection and analysis of field data. We are also grateful to Jim Thompson, Kent Hathaway, and the USACE-FRF staff, for providing in situ observational data. John Stanley and Adam Keen assisted with Argus data processing. Dan Clark designed and deployed the IR sampling system. Gabriel Garcia assisted with numerical modeling. Wilson also wishes to thank the organizers and participants of the 2012 Les Houches summer school, as well as Bob Miller and Alex Kurapov, for many interesting discussions on data assimilation. Data used for producing the results herein may be requested by contacting the authors.

References

Aksoy, A., F. Zhang, and J. W. Nielsen-Gammon (2006), Ensemble-based simultaneous state and parameter estimation in a two-dimensional sea-breeze model, *Mon. Weather Rev.*, *134*, 2951–2970.

Allard, R., J. Dykes, Y. L. Hsu, J. Kaihatu, and D. Conley (2008), A real-time nearshore wave and current prediction system, *J. Mar. Syst.*, *69*, 37–58.

Austin, M. J., T. M. Scott, P. E. Russell, and G. Masselink (2012), Rip current prediction: Development, validation, and evaluation of an operational tool, *J. Coastal Res.*, *29*, 283–300.

Battjes, J. A., and J. P. F. M. Janssen (1978), Energy loss and set-up due to breaking of random waves, in *Proceedings of the 16th International Coastal Engineering Conference*, pp. 570–587, Am. Soc. of Civ. Eng., New York.

Béal, D., P. Brasseur, J. M. Brankart, Y. Ourmières, and J. Verron (2010), Characterization of mixing errors in a coupled physical biogeochemical model of the North Atlantic: Implications for nonlinear estimation using Gaussian anamorphosis, *Ocean Sci.*, *6*, 247–262.

Bennett, A. F. (2002), *Inverse Modeling of the Ocean and Atmosphere*, Cambridge Univ. Press, New York.

Birkemeier, W. A. (1984), The CRAB: A unique nearshore surveying vehicle, *J. Surv. Eng.*, *110*, 1–7.

Blenkinsopp, C. E., I. L. Turner, M. J. Allis, W. L. Peirson, and L. E. Garden (2012), Application of LIDAR technology for measurement of time-varying free-surface profiles in a laboratory wave flume, *Coastal Eng.*, *68*, 1–5.

Bocquet, M., C. A. Pires, and L. Wu (2010), Beyond Gaussian statistical modeling in geophysical data assimilation, *Mon. Weather Rev.*, *138*, 2997–3023.

Booij, N., R. C. Ris, and L. H. Holthuijsen (1999), A third-generation wave model for coastal regions. 1: Model description and validation, *J. Geophys. Res.*, *104*(C4), 7649–7666.

Catalán, P. A., and M. C. Haller (2007), Remote sensing of breaking wave phase speeds with application to non-linear depth inversions, *Coastal Eng.*, *55*, 93–111.

Catalán, P. A., M. C. Haller, R. A. Holman, and W. J. Plant (2011), Optical and microwave detection of wave breaking in the surf zone, *IEEE Trans. Geosci. Remote Sens.*, *49*, 1879–1893.

Chickadel, C. C., R. A. Holman, and M. H. Freilich (2003), An optical technique for the measurement of longshore currents, *J. Geophys. Res.*, *108*(C11), 3364, doi:10.1029/2003JC001774.

Chickadel, C. C., A. R. Horner-Devine, S. A. Talke, and A. T. Jessup (2009), Vertical boil propagation from a submerged estuarine sill, *Geophys. Res. Lett.*, *36*, L10601, doi:10.1029/2009GL037278.

de Vries, S., D. F. Hill, M. A. de Schipper, and M. J. F. Stive (2011), Remote sensing of surf zone waves using stereo imaging, *Coastal Eng.*, *58*, 239–250.

Dee, D. P. (1995), On-line estimation of error covariance parameters for atmospheric data assimilation, *Mon. Weather Rev.*, *123*, 1128–1145.

Dugan, J. P., C. C. Piotrowski, and J. Z. Williams (2001), Water depth and surface current retrievals from airborne optical measurements of surface gravity wave dispersion, *J. Geophys. Res.*, *106*(C8), 16,903–16,915.

Evensen, G. (2006), *Data Assimilation: The Ensemble Kalman Filter*, Springer, Berlin.

Evensen, G., and P. J. van Leeuwen (1996), Assimilation of Geosat altimeter data for the Agulhas current using the ensemble Kalman filter with a quasigeostrophic model, *Mon. Weather Rev.*, *124*, 85–96.

Feddersen, F., and R. T. Guza (2003), Observations of nearshore circulation: Alongshore uniformity, *J. Geophys. Res.*, *108*(C1), 3006, doi:10.1029/2001JC001293.

Feddersen, F., R. T. Guza, and S. Elgar (2004), Inverse modeling of one-dimensional setup and alongshore current in the nearshore, *J. Phys. Oceanogr.*, *34*, 920–933.

Haas, K. A., and I. A. Svendsen (2002), Laboratory measurements of the vertical structure of rip currents, *J. Geophys. Res.*, *107*(C5), 3047, doi:10.1029/2001JC000911.

Haas, K. A., and J. C. Warner (2009), Comparing a quasi-3D to a full 3D nearshore circulation model: SHORECIRC and ROMS, *Ocean Modell.*, *26*, 91–103.

Haas, K. A., I. A. Svendsen, and M. C. Haller (1998), Numerical modeling of nearshore circulation on a barred beach with rip channels, in *Proceedings of the 26th International Coastal Engineering Conference*, vol. 1, pp. 801–814, Am. Soc. of Civ. Eng, Copenhagen, Denmark.

Haas, K. A., I. A. Svendsen, M. C. Haller, and Q. Zhao (2003), Quasi-three-dimensional modeling of rip current systems, *J. Geophys. Res.*, *108*(C7), 3217, doi:10.1029/2002JC001355.

Haller, M. C., D. Honegger, and P. A. Catalán (2013), Rip current observations via marine radar, *J. Waterw. Port Coastal Ocean Eng.*, *140*(2), 115–124, doi:10.1061/(ASCE)WW.1943–5460.0000229.

Hamill, T. M., and J. S. Whitaker (2005), Accounting for the error due to unresolved scales in ensemble data assimilation: A comparison of different approaches, *Mon. Weather Rev.*, *133*, 3132–3147.

Hamill, T. M., J. S. Whitaker, and C. Snyder (2001), Distance-dependent filtering of background error covariance estimates in an ensemble Kalman filter, *Mon. Weather Rev.*, *129*, 2776–2790.

Holland, K. T., J. A. Puleo, and T. N. Kooney (2001), Quantification of swash flows using video-based particle image velocimetry, *Coastal Eng.*, *44*, 65–77.

Holman, R. A., and M. C. Haller (2013), Remote sensing of the nearshore, *Ann. Rev. Mar. Sci.*, *5*, 95–113.

Holman, R. A., and J. Stanley (2007), The history and technical capabilities of Argus, *Coastal Eng.*, *54*, 477–491.

Holman, R. A., N. G. Plant, and K. T. Holland (2013), cBathy: A robust algorithm for estimating nearshore bathymetry, *J. Geophys. Res.*, *118*, 2595–2609, doi:10.1002/jgrc.20199.

Houtekamer, P. K., and H. L. Mitchell (1998), Data assimilation using an ensemble Kalman filter technique, *Mon. Weather Rev.*, *126*, 796–811.

Houtekamer, P. L., H. L. Mitchell, and D. Xingxiu (2008), Model error representation in an operational ensemble Kalman filter, *Mon. Weather Rev.*, *137*, 2126–2143.

Jessup, A., R. A. Holman, C. Chickadel, S. Elgar, G. Farquharson, M. C. Haller, A. L. Kurapov, H. T. Özkan- Haller, B. Raubenheimer, and J. M. Thomson (2012), DARLA: Data Assimilation and Remote Sensing for Littoral Applications, (Invited) Abstract OS14A-01 presented at 2012 Fall Meeting, AGU, San Francisco, Calif., 3–7 Dec.

Kirby, J. T., and R. A. Dalrymple (1986), An approximate model for nonlinear dispersion in monochromatic wave propagation models, *Coastal Eng.*, *9*, 545–561.

Kumar, N., G. Voulgaris, and J. C. Warner (2011), Implementation and modification of a three-dimensional radiation stress formulation for surf zone and rip-current applications, *Coastal Eng.*, *58*, 1097–1117.
Kumar, N., G. Voulgaris, J. C. Warner, and M. Olabarrieta (2012), Implementation of the vortex force formalism in the coupled ocean-atmosphere-wave-sediment transport (COAWST) modeling system for inner shelf and surf zone applications, *Ocean Modell.*, *47*, 65–95.
Kurapov, A. L., and H. Özkan-Haller (2013), Bathymetry correction using an adjoint component of a coupled nearshore wave-circulation model: Tests with synthetic velocity data, *J. Geophys. Res.*, *118*, 4673–4688, doi:10.1002/jgrc.20306.
Landon, K. C., G. W. Wilson, H. T. Özkan-Haller, and J. H. MacMahan (2013), Bathymetry estimation using drifter-based velocity measurements on the Kootenai River, ID, USA, *J. Atmos. Oceanic Technol.*, *31*, 503–514, doi:10.1175/JTECH-D-13-00123.1.
Lentz, S., R. T. Guza, S. Elgar, F. Feddersen, and T. H. C. Herbers (1999), Momentum balances on the North Carolina inner shelf, *J. Geophys. Res.*, *104*(C8), 18,205–18,226.
Li, H., E. Kalnay, and T. Miyoshi (2009), Simultaneous estimation of covariance inflation and observation errors within an ensemble Kalman filter, *Q. J. R. Meteorol. Soc.*, *135*, 523–533.
Lippmann, T. C., and R. A. Holman (1990), The spatial and temporal variability of sand bar morphology, *J. Geophys. Res.*, *95*(C7), 11,575–11,590.
Long, C. E. (1996), Index and bulk parameters for frequency-directional spectra measured at CERC Field Research Facility, July 1994 to August 1995, *Misc. Pap. CERC-96-6*, U.S. Army Eng. Waterw. Exp. Stn., Vicksburg, Miss.
Mei, C. C. (1983), *The Applied Dynamics of Ocean Surface Waves*, John Wiley, New York.
Mulligan, R. P., J. L. Hanson, and K. K. Hathaway (2010), Observations of wave breaking and surf zone width from a real-time cross-shore array of wave and current sensors at Duck, NC, in *2011 IEEE/OES 10th Current, Waves and Turbulence Measurements (CWTM 2011)*, 130–137, doi: 10.1109/CWTM.2011.5759540.
Palmsten, M. L., and R. A. Holman (2011), Laboratory investigation of dune erosion using stereo video, *Coastal Eng.*, *60*, 123–135.
Plant, N. G., and R. A. Holman (1997), Intertidal beach profile estimation using video images, *Mar. Geol.*, *140*, 1–24.
Plant, N. G., K. T. Holland, and J. A. Puleo (2002), Analysis of the scale of errors in nearshore bathymetric data, *Mar. Geol.*, *191*, 71–86.
Plant, N. G., K. T. Holland, and M. C. Haller (2008), Ocean wavenumber estimation from wave-resolving time series imagery, *IEEE Trans. Geosci. Remote Sens.*, *46*, 2644–2658.
Plant, N. G., K. L. Edwards, J. M. Kaihatu, J. Veeramony, L. Hsu, and K. T. Holland (2009), The effect of bathymetric filtering on nearshore process model results, *Coastal Eng.*, *56*, 484–493.
Puleo, J. A., G. Farquharson, S. J. Frasier, and K. T. Holland (2003), Comparison of optical and radar measurements of surf and swash zone velocity fields, *J. Geophys. Res.*, *108*(C3), 3100, doi:10.1029/2002JC001483.
Reniers, A. J. H. M., J. A. Roelvink, and E. B. Thornton (2004), Morphodynamic modeling of an embayed beach under wave group forcing, *J. Geophys. Res.*, *109*, C01030, doi:10.1029/2002JC001586.
Ruessink, B. G., J. R. Miles, F. Feddersen, R. T. Guza, and S. Elgar (2001), Modeling the alongshore current on barred beaches, *J. Geophys. Res.*, *106*(C10), 22,451–22,463.
Shchepetkin, A. F., and J. C. McWilliams (2005), The regional oceanic modeling system (ROMS): A split-explicit, free-surface, topography-following-coordinate oceanic model, *Ocean Modell.*, *9*, 347–404.
Smith, S. D. (1988), Coefficients for sea surface wind stress, heat flux, and wind profiles as a function of wind speed and temperature, *J. Geophys. Res.*, *93*(15), 467–415.
Svendsen, I. A. (1984), Wave heights and set-up in a surf zone, *Coastal Eng.*, *8*, 303–329.
Svendsen, I. A., and U. Putrevu (1990), Nearshore circulation with 3-D profiles, in *Proceedings of the 22nd International Coastal Engineering Conference*, edited by B. Edge, pp. 241–254, Am. Soc. of Civ. Eng., New York.
Uchiyama, Y., J. C. McWilliams, and A. F. Shchepetkin (2010), Wave-current interaction in an oceanic circulation model with a vortex-force formalism: Application to the surf zone, *Ocean Modell.*, *34*, 16–35.
van Dongeren, A., N. Plant, A. Cohen, D. Roelvink, M. C. Haller, and P. Catalán (2008), Beach Wizard: Nearshore bathymetry estimation through assimilation of model computations and remote observations, *Coastal Eng.*, *55*, 1016–1027.
Veeramony, J., D. Walker, and L. Hsu (2010), A variational data assimilation system for nearshore applications of SWAN, *Ocean Modell.*, *35*, 206–214.
Wilson, G. W., and H. T. Özkan-Haller (2012), Ensemble-based data assimilation for estimation of river depths, *J. Atmos. Oceanic Technol.*, *29*, 1558–1568.
Wilson, G. W., H. T. Özkan-Haller, and R. A. Holman (2010), Data assimilation and bathymetric inversion in a 2DH surf zone model, *J. Geophys. Res.*, *115*, C12057, doi:10.1029/2010JC006286.
Yu, J., and D. N. Slinn (2003), Effects of wave-current interaction on rip currents, *J. Geophys. Res.*, *108*(C3), 3088, doi:10.1029/2001JC001105.
Zaron, E. D., M. A. Pradal, P. D. Miller, A. F. Blumberg, N. Georgas, W. Li, and J. Muccino Cornuelle (2011), Bottom topography mapping via nonlinear data assimilation, *J. Atmos. Oceanic Technol.*, *28*, 1606–1623.

